Synergistic effects of the hybridization between boron-doped carbon quantum dots and n/n-type g-C_3N_4 homojunction for boosted visible-light photocatalytic activity

Synergistic effects of the hybridization between boron-doped carbon quantum dots and n/n-type g-C_3N_4 homojunction for boosted visible-light photocatalytic activity

Sue Jiun Phang [a], Jiale Lee [b], Voon-Loong Wong [a], Lling-Lling Tan [b*], Siang-Piao Chai [b]

[a] School of Engineering and Physical Sciences, Heriot-Watt University Malaysia, Jalan Venna P5/2, Precinct 5, 62200 Putrajaya, Malaysia

[b] Multidisciplinary Platform of Advanced Engineering, Chemical Engineering Discipline, School of Engineering, Monash University, Jalan Lagoon Selatan, 47500 Bandar Sunway, Selangor, Malaysia

Acknowledgements

This work was funded by the Ministry of Higher Education (MOHE) Malaysia under the Fundamental-Research Grant Scheme (FRGS) (Ref no: FRGS/1/2018/TK02/HWUM/03/2).

*Corresponding author
Dr. Lling-Lling Tan
E-mail: tan.llinglling@monash.edu
Telephone: +6 03 5514 4901

Abstract

Dye wastewater has raised a prevalent environmental concern due to its ability to prevent the penetration of sunlight through water, thereby causing a disruption to the aquatic ecosystem. Carbon quantum dots (CQDs) are particularly sought after for their highly tailorable photoelectrochemical and optical properties. Simultaneously, graphitic carbon nitride (g-C_3N_4) has gained widespread attention due to its suitable band gap energy as well as excellent chemical and thermal stabilities. Herein, a novel boron-doped CQD (BCQD) hybridized g-C_3N_4 homojunction (CN) nanocomposite was fabricated via a facile hydrothermal route. The optimal photocatalyst sample, 1-BCQD/CN (with a 1:3 mass ratio of boron to CQD) accomplished a Rhodamine B (RhB, 10 mg/L) degradation efficiency of 97.0 % within 4 hours under an 18 W LED light irradiation. The kinetic rate constant of 1.39 x 10^{-2} min^{-1} achieved by the optimum sample was found to be 3.6- and 2.8-folds higher than that of pristine CN and un-doped CQD/CN, respectively. The surface morphology, crystalline structure, chemical composition and optical properties of photocatalyst samples were characterized via TEM, FESEM-EDX, XRD, FTIR, UV-Vis DRS and FL spectrometer. Based on the scavenging tests, it was revealed that the photogenerated holes (h^+), superoxide anions ($\cdot O_2^-$) and hydroxyl radicals ($\cdot$OH) were the primary reactive species responsible for the photodegradation process. Overall, the highly efficient 1-BCQD/CN composite with excellent photocatalytic activity could provide a cost-effective and robust means to address the increasing concerns over global environmental pollution.

Keyword(s): Photocatalysis; carbon quantum dots; graphitic carbon nitride; wastewater treatment

1.0 Introduction

In the recent years, the dramatic growth in global population calls for immediate measures to protect the environment and natural resources. While the rapid industrialization has indeed promoted the blooming of various sectors including food and beverage, paper and textile, irrigation and drainage, medical and pharmaceutical, etc., these industries are accountable for several major environmental issues. In this regard, the discharge of effluents by these production and manufacturing plants is detrimental to Mother Nature, resulting in the pollution of water resources and diminished water quality. Notably, the level of dissolved contaminants in the vast majority of water bodies is above the acceptable standard for human consumption, leading to the scarcity of clean water in many communities around the world. Based on data from the World Health Organization, an annual estimation of 485,000 diarrheal deaths occur due to the consumption of contaminated drinking water while waterborne diseases such as cholera, polio and typhoid remain as serious threats to the public health (Organization, 2019). Specifically for wastewater containing azo dyes, it induces mutagenic and carcinogenic effects with the presence of complex aromatic compounds (da Silva et al., 2014). The high color intensity displayed by organic dyes also jeopardizes the aquatic ecology as it impedes the sunlight from entering the water, resulting in reduced photosynthesis and consequently eutrophication. Therefore, an effective, sustainable and environmentally-benign method to treat dye-containing wastewater is of utmost importance.

Photocatalysis has garnered widespread attention amongst researchers as this cutting-edge technology is highly green and sustainable. The advanced oxidation processes (AOPs) offered by heterogeneous photocatalysis is especially promising because of its ability to oxidize a wide spectrum of complex organic compounds, attributing to highly reactive oxidants as well as reactive species with relatively low selectivity such as the hydroxyl radicals (Ma et al., 2014; Muraro et al.,

2020). Photocatalyst is broadly recognized for its robustness and versatile applicability across different fields including mineralization of organic pollutants, CO_2 reduction, hydrogen generation via water splitting and others (Moreno et al., 2021; Zhen et al., 2021). While water treatment by means of photo-driven reactions is undoubtedly environmentally friendly, the performances of the existing photocatalytic systems are greatly hampered by several setbacks. Among the prominent issues include the ineffective utilization of solar energy and the rapid recombination rate of electron-holes pairs (Weon et al., 2019; Jiao et al., 2020). As visible light makes up an approximately 42 % of the solar energy, the design of a visible-light-responsive photocatalyst is greatly desired due to its relatively high photonic energy (Wang et al., 2017c). Hitherto, most of the existing photocatalytic systems are only active under high energy ultraviolet (UV) light which constitutes merely 6 % of the entire solar spectrum (An et al., 2016). A number of strategies such as functionalization, elemental doping and size tuning have been proposed to boost the apparent quantum efficiency of the existing photocatalysts and concurrently diminish the aforementioned limitations (Nassar and Abdelrahman, 2017; Ma et al., 2018; Li et al., 2020b). A plethora of nanomaterials have also been identified as promising photocatalytic materials. These include metallic titanium oxide (TiO_2), tungsten oxide (WO_3), MXenes as well as non-metallic CQDs, graphitic carbon nitride (g-C_3N_4), phosphorus (P), graphene and combinations hereof (Cushing et al., 2017; Cao et al., 2018; Jeevitha et al., 2018; Hu et al., 2019; Kooshki et al., 2019; Mishra et al., 2019).

Ascribing to its suitable electronic band structure, facile synthesis and readily tunable features, two-dimensional (2D) g-C_3N_4 has thrust into the limelight within the field of photocatalysis (Che et al., 2019). As compared to its metal-based counterparts, the metal-free g-C_3N_4 has also alleviated the risk of metal-leaching, which is known to be a process where toxic

metal components dissolve into liquid medium, inflicting detrimental damage to the environment (Zhang et al., 2016b; Sahu et al., 2020). The vast untapped potential of g-C_3N_4 has prompted much research interests in studying its structural framework, optoelectronic and physicochemical properties. Among the more effective strategies in enhancing the photocatalytic performance of g-C_3N_4 is through the formation of a homojunction system, where the difference in conduction band (CB) and valence band (VB) levels between precursors could facilitate the separation of photoinduced charge carriers (Phang et al., 2020b). Several research articles on g-C_3N_4 homojunction with enhanced photocatalytic performance have been published in literature (Ye et al., 2017; Phang et al., 2020a). For instance, Tan et al. successfully fabricated a mesoporous g-C_3N_4 nanosheets laminated homojunction, which displayed a 12.5- and 6.5-fold improvement in performance as compared to pristine g-C_3N_4 derived from melamine and amino cyanamide respectively (Tan et al., 2017). Similarly, Yang's group constructed a triazine-/heptazine-based g-C_3N_4 homojunction via the overgrowth of triazine-based g-C_3N_4 nanoparticles embedded on the inner wall of the heptazine-based g-C_3N_4 hollow tubes (Yang et al., 2020a). The efficiency for photocatalytic H_2 generation was drastically improved, with a H_2 evolution rate 12-times higher in relative to bulk g-C_3N_4. On the whole, the ameliorated photoactivities in different applications are primarily credited to the enhanced photo-response towards visible light, rapid charge transfer and separation in addition to excellent photo-stability upon the formation of homojunction structures.

To further improve the photoactivity of g-C_3N_4, the doping of a co-catalyst onto the fundamental framework is regarded as one of the most effective strategies (Ran et al., 2015; Chen et al., 2017; Hasija et al., 2019). Carbon quantum dots (CQDs) are widely known as a novel class of nanomaterials with ultrafine dimensions of less than 10 nm (Phang and Tan, 2019). CQDs have

become the focus of attention among material scientists and researchers in the recent years owing to their prominent optical and physicochemical properties. Furthermore, CQDs are also highly sought after for its up-converted photoluminescence (UCPL) properties, extended range of sensitivity towards visible light as well as its inexpensive synthesis cost (Wang et al., 2019a; Molaei, 2020). The readily tunable features of CQDs, chemically and physically, renders their robustness and allow them to be tailored precisely for a variety of applications. Recently, there has been a surge in publications on the modification strategies of CQDs to further enhance their photocatalytic effectiveness. These strategies include size tuning for quantum confinement effect (Li and Zhao, 2014), surface passivation and functionalization (Luo et al., 2013; Lim et al., 2015; Yang et al., 2016; Pan et al., 2017), heteroatom doping and the formation of hybridized nanocomposites (Ma et al., 2016; Zhang et al., 2017a). Among the common doping elements for CQDs are nitrogen (N), boron (B), sulfur (S), phosphorus (P), which are typically derived from urea, boric acid, L-cysteine and phosphoric acid, respectively (Bhati et al., 2019; Lin et al., 2019; Wang et al., 2019b; Zhang et al., 2020b). Each element has its distinctive advantages over the other elements in improving the photoactivity of CQDs. For instance, N-doped CQDs were reported to increase the aqueous dispersibility and fluorescence emission of the composite while B-doped CQDs displayed enhanced visible light absorption and quantum yield (Ma et al., 2012; Guo et al., 2018; Song et al., 2020). On the other hand, doping of heteroatom S was shown to improve the electrical conductivity of CQDs whereas the introduction of P dopants accelerated the electron transfer to impede charge carrier recombination (Wang et al., 2019b; Zhang et al., 2020c). Collectively, it is apparent that the doping of CQDs with different heteroatoms are promising to drastically enhance various extrinsic properties and structural features advantageous for photocatalysis. For instance, Peng et al. successfully fabricated the B-doped carbon dots via a

simple hydrothermal route. Based on the photoactivity test over RhB and methylene blue (MB) degradation. The synthesized B-doped carbon dots demonstrated an outstanding performance in which a 100% degradation of both dyes were attained within a short span of 170 minutes (Peng et al., 2020).

In this work, we report the smart engineering of zero-dimensional (0D) B-doped CQD (BCQD) on 2D g-C_3N_4/g-C_3N_4 homojunction (CN) to form a highly robust hybrid BCQD/CN. To the best of our knowledge, the fabrication of this novel and efficient nanocomposite system for RhB degradation has not been reported in literature thus far. Herein, BCQDs were doped onto CN via a facile hydrothermal method. The CQDs were derived from citric acid with boric acid as the B-dopant, while g-C_3N_4 homojunctions were fabricated with urea and thiourea as the precursors. The mass loadings of boric acid were varied to determine the optimum amount of B-dopant over the n/n-junctioned g-C_3N_4. The photocatalytic efficiency of the as-developed photocatalyst samples were evaluated via the degradation of RhB dye. It is noteworthy that the present work employs the use of a low-powered 18 W LED light as the irradiation source, rendering the overall photocatalytic process both environmentally benign and economically feasible. All in all, this study aims to provoke novel research ideas in the field of photocatalysis with the development of BCQDs incorporated g-C_3N_4/g-C_3N_4 homojunction nanocomposites.

2.0 Experimental

2.1 Materials

Citric acid (99.5 %, MW= 192.12 g/mol), urea (99.5 %, MW= 60.06 g/mol), thiourea (98%, MW= 76.12 g/mol) and p-benzoquinone (BZQ, 98 %, MW= 108.10 g/mol) were purchased from R&M Chemicals, UK. Boric acid (99.5 %, MW= 61.83 g/mol) was purchased from Merck KGaA, Germany. Rhodamine B dye (RhB, 98.5 %, MW= 479.02 g/mol, pKa= 4.2), triethanolamine

(TEOA, 99 %, MW= 149.19 g/mol) and 2-propanol (IPA, 99 %, MW= 60.1 g/mol) were obtained from QReC̈ (Asia) Sdn. Bhd., Malaysia. Distilled water was employed throughout the experiments. All reagents were of analytical grade (AR) and applied without further purification.

2.2 Preparation of photocatalysts

2.2.1 Synthesis of BCQD

Three (3) grams of citric acid and *x*-amount of boric acid were mixed in 15 ml of distilled water followed by mild stirring for 10 min. The symbol '*x*' denotes the amount of boron-dopant employed (0.5, 1, 2 and 3 g) in the synthesis of BCQDs with respect to a fixed amount of CQDs. The homogeneous mixture was then transferred into a Teflon-lined autoclave reactor for hydrothermal treatment at 180 $^{\circ}$C for 14 hrs, after which the solution was cooled naturally to ambient temperature. Subsequently, the resultant brown suspension was subjected to centrifugation at 12,000 rpm for 20 min to remove larger particles and impurities. The supernatant containing purified BCQD was obtained and dried in an oven at 90 $^{\circ}$C overnight before further use. The prepared samples with 0.5, 1, 2 and 3 g of boric acid were denoted as 0.5-BCQD, 1-BCQD, 2-BCQD and 3-BCQD respectively. Pristine CQD samples were also synthesized following a similar procedure without the addition of boric acid.

2.2.2 Synthesis of g-C_3N_4/g-C_3N homojunction (CN)

g-C_3N_4/g-C_3N_4 homojunction was prepared by a facile thermal polymerization route following a reported work with slight modifications (Phang et al., 2020a). Typically, 6 g of each precursor (urea and thiourea) were mixed in 30 ml of distilled water with gentle stirring to obtain a well-mixed solution. Subsequently, the resultant mixture was placed in the oven at 90 $^{\circ}$C overnight to construct the nanocomposite photocatalyst. The molecular composite was transferred into a porcelain crucible and subjected to calcination at 550 $^{\circ}$C with a ramping rate of 2 $^{\circ}$C/min for 2 hrs.

The resultant yellow-colored solid was cooled to ambient temperature overnight and then ground to fine powders before further use.

2.2.3 Synthesis of BCQD/CN nanocomposite

One (1) gram of the as-synthesized CN and 0.01 g (1 wt %) of pristine CQD or *x*-BCQD were mixed in 90 ml and 10 ml of distilled water respectively. The two solutions undergone ultrasonication in separate beakers for 30 min to minimize agglomeration and exfoliate the layers of g-C_3N_4 nanosheets. Next, both solutions were mixed and stirred for 30 min. The resultant beige-colored solution was transferred into a Teflon-lined autoclave reactor and heated at 120 ˚C for 4 hrs. The sample was collected via filtration and washed with distilled water several times. Finally, the nanocomposite photocatalyst was obtained after oven-drying at 70 ºC overnight. The final photocatalyst samples were labelled as CQD/CN, 0.5-BCQD/CN, 1-BCQD/CN, 2-BCQD/CN and 3-BCQD/CN. The synthesis route of BCQD/CN nanocomposites is depicted in Fig. 1.

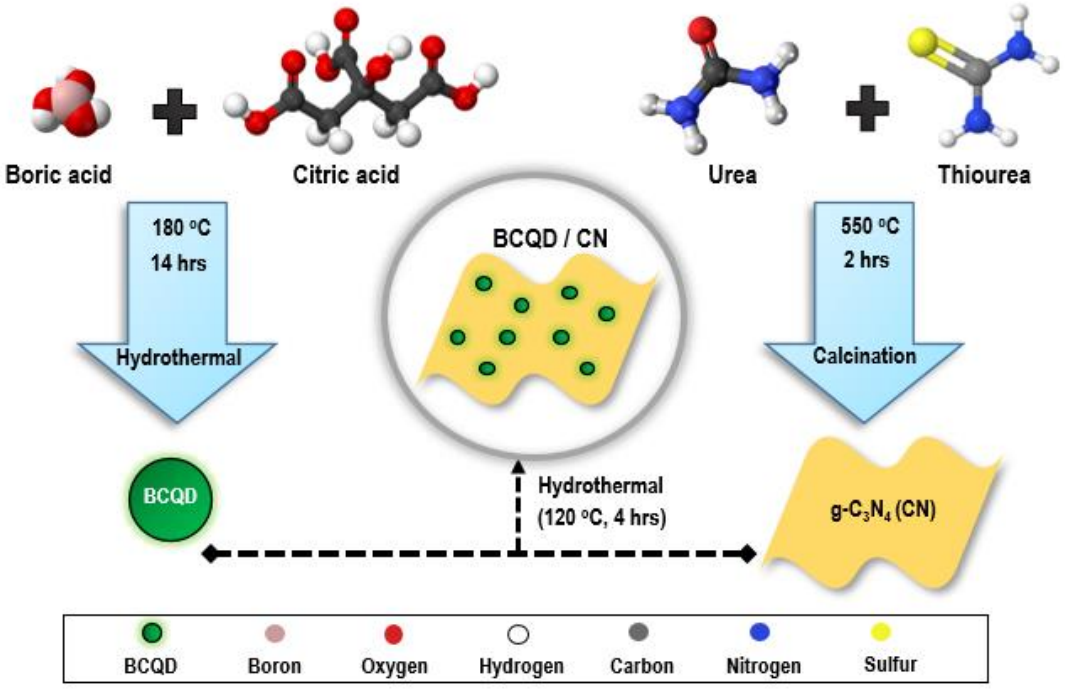

Fig. 1 Schematic illustration of synthesis route for BCQD/CN nanocomposites

2.3 Characterization of materials

The surface morphology of CQD/CN and the optimized photocatalyst sample, 1-BCQD/CN were analyzed with transmission electron microscopy (TEM) (FEI Tecnai G2 20 S-TWIN, USA) by applying 200 kV of accelerating voltage. Field emission scanning electron microscope (FE-SEM) (ultra-high-resolution Hitachi SU8010, Japan) coupled with energy dispersive X-ray analyzer (EDX) were carried out to study the surface morphology, elemental compositions and framework of CN, CQD/CN and 1-BCQD/CN. For TEM and FESEM analysis, a small amount of the photocatalyst samples were dispersed in ethanol solution and subjected to 1 min of ultra-sonication, the suspension was then dropped on a lacey carbon film and silicon wafer respectively. The lacey carbon film and silicon wafer were subsequently oven-dried prior to TEM and FESEM characterization. EDX analysis was performed quantitatively for spatial variations in elemental compositions through spot scans. The crystal structures of CN, CQD/CN and 1-BQD/CN were characterized via high resolution X-ray diffraction (XRD) with X-ray diffractometer (Bruker D8 Discover, Germany) in the presence of Ni-filtered Cu Kα operated at 40 kV and 40 mA, with 0.02 ^{o}/s as scanning rate. XRD peaks are developed by constructive interference of a monochromatic beam of X-rays and described by Bragg's Law: $n\lambda = 2d \sin\theta$, where order of reflection, wavelength of incident X-rays, interplanar spacing of crystal and incident angle are denoted by n, λ, d and θ respectively. Fourier Transform Infrared (FTIR) spectra of CN, CQD/CN and 1-BCQD/CN were measured with FTIR spectrometer (Perkin Elmer Frontier) based on percent transmittance (% T) value in the wavenumber range of 4000 - 400 cm^{-1} and resolution of 1 cm^{-1}. Ultraviolet-visible diffuse reflectance spectra (UV-vis DRS) of the as-developed photocatalyst samples were analyzed using Cary 100 UV-Vis (Agilent Technologies, USA). All optical evaluations were obtained at

room temperature and pressure with a wavelength range of 300 – 800 nm. Photoluminescence (PL) spectra of the samples were recorded with fluorescence spectrometer (Perkin Elmer LS-55, USA) with 420 nm as measurement wavelength.

2.4 Photocatalytic activity evaluation

The photoactivity of as-prepared samples were assessed via the degradation of a cationic dye, Rhodamine B (RhB). The photocatalytic experiments were conducted in a homemade photoreactor under ambient conditions. Typically, 0.15 g of photocatalyst sample was uniformly distributed in a glass beaker containing 100 mL of 10 mg/L RhB solution. The resultant mixture was stirred without light for 30 min to establish adsorption-desorption equilibrium. Before switching on the light source, a 5 ml aliquot of the equilibrated RhB solution was collected and used as the blank sample. The LED lamp (4410R-18W) was then switched on as the source of irradiation and samples were obtained at every 60-min interval for a total duration of 240 min. The range of wavelength and intensity of LED light source employed are 400 – 700 nm and 0.237 W/m^2 respectively. All solution samples were subjected to centrifugation at 12,000 rpm for 3 mins for removal of suspended powdered photocatalyst. The supernatant was then obtained and measured using a UV-Vis spectrophotometer (Hach DR 6000) and a wavelength scan ranging from 300 – 800 nm was obtained. The characteristic peak of the absorption band for RhB dye (552 nm) was also recorded with respect to time. Pseudo first rate constant, k of the photo-reaction was determined following the Langmuir-Hinshelwood model as presented in Equation 1, where C_0 (mg/L), C (mg/L), k (min^{-1}) and *t* (min) denote the RhB concentration at time *t*, initial concentration, kinetic rate constant and irradiation time, respectively.

$$ln\frac{C_o}{C} = k \times t \qquad (1)$$

The efficiency of the photocatalyst samples was evaluated in accordance with Equation 2:

$$Degradation\ efficiency, DE = \frac{C_o - C}{C_o} \times 100\% \quad (2)$$

A standard equilibrium curve was constructed to establish a correlation between the absorbance and the concentration of RhB dye conforming to the Beer-Lambert Law, which proclaims that the concentration and absorption of a species in the solution is proportional to one another.

2.5 Photoelectrochemical measurement

Photoelectrochemical characterizations of the photocatalysts were analyzed with an electrochemical workstation (CHI 6005E, Chenhua Instruments, China) in a quartz cell equipped with a standard three-electrode system. Each sample was coated on a titanium electrode and employed as the working electrode. Meanwhile, a Pt plate and saturated Ag/AgCl electrode were employed as the counter and reference electrode respectively. 0.003 mg of photocatalyst sample was distributed in C_2H_5OH and ultrasonicated for 10 mins prior to drop-casting the catalyst onto a 1 cm^2 fluorine-doped tin oxide (FTO) substrate. The film was subsequently oven-dried and the thin-film electrodes of CN, CQD/CN and 1-BCQD/CN were obtained. A 1.0 M Na_2SO_4 was employed as the electrolyte. The evaluation of transient photocurrent response was carried out with the light being switched on and off by applying a bias of 0.35 V. The electrochemical impedance spectra (EIS) were evaluated over a frequency of 0.1 – 10^5 Hz and applied potential of 0.35 V vs. Ag/AgCl with an alternating current (AC) perturbation signal of 0.01 V under the irradiation of visible light ($\lambda > 400$ nm). The Mott-Schottky plot of photocatalyst samples were obtained over a potential range of –1.0 to 1.0 V vs. Ag/AgCl.

2.6 Free radical scavenging tests

To investigate the photocatalytic mechanisms underlying BCQD/CN nanocomposites, a series of scavenging tests were conducted. 2-propanol (IPA), triethanolamine (TEOA) and p-benzoquinone (BZQ) were utilized to capture hydroxyl (·OH), holes (h^+) and superoxide anion ($\cdot O_2^-$) radicals respectively. The concentrations of IPA and TEOA used in the scavenging tests was fixed at 1.2 vol %; while 0.6 vol % of BZQ was employed. The experimental setup for the scavenging analysis was identical to the procedure of photocatalytic activity evaluation as presented in Section 2.4.

2.7 Point of zero charge (pH_{pzc}) measurement

The pH_{pzc} of the photocatalyst sample was determined using the pH drift method at room temperature with 0.15 g of photocatalyst dispersed in 100 mL of NaCl solution (0.01 M) (Zhang et al., 2014). The initial pH values were adjusted between the range of 3 – 11 with HCl (0.01 M) and NaOH (0.01 M). The photocatalyst-NaCl suspensions were placed in a shaker for 24 hrs to equilibrate the process of proton adsorption-desorption. The equilibrium/final pH value was then measured and plotted against the initial pH value. The pH_{pzc} of the corresponding photocatalyst was determined as the intersection point of initial and equilibrium pH.

2.8 Process optimization of RhB photodegradation by Response Surface Methodology (RSM)

RSM is an established technique applied in the process optimization of a multivariable system (Vaez et al., 2012). The optimal conditions for photodegradation of RhB was determined using Minitab 19 statistical software. In this study, the three independent parameters of interest are pH value (x_1), initial concentration of dye (x_2) and dosage of photocatalyst (x_3), corresponding to the degradation efficiency of RhB as the response. The set level and range of the independent variables are tabulated in Table 1.

Table 1. Experimental level and range of the independent parameters

Variables	Level and range		
	-1	0	+1
pH value, x_1	3	7	11
Initial dye concentration, x_2 (mg/L)	10	20	30
Photocatalyst dosage, x_3 (g)	0.10	0.15	0.20

The form of RSM used in this study is Box-Behnken designs (BBD) to evaluate the effect of three independent variables in 13 sets of experimental runs according to the following equation:

$$N = 2 \times K\,(K-1) + \theta \qquad (3)$$

Where K and Θ are the number of factors and points in the center respectively.

3.0 Results and discussion

3.1 Characterization of CN, CQD/CN and 1-BCQD/CN

The surface structure and morphology of CN, CQD/CN and 1-BCQD/CN were analyzed using FESEM and TEM. The successful fabrication of an n/n-type g-C_3N_4 homojunction (CN) was reported in our previous work (Phang et al., 2020a). As shown in Fig. 2(a), the FESEM image of CN features two-dimensional (2D) nanosheets with wide lateral dimensions. The formation of macro-scale g-C_3N_4 was due to the stacking of 2D polymer molecules while the lamellar structure of g-C_3N_4 was eventually produced as the planar structure of the molecules undergone distortion. Such distortion was reported to be a result of the enlarged space between g-C_3N_4 polymer molecules developed during the release of ammonia gas during the calcination step (Song et al., 2020). In addition, the platelet-like structures were also observed to be highly porous with large spatial networks. Fig. 2(b) and 2(c) illustrate the FESEM images of CQD/CN and 1-BCQD/CN. From the microscopy images, it is evident that the 2D nanosheet framework of g-C_3N_4 was generally well-retained. This indicated that the introduction of CQDs and BCQDs had no

substantial effects on the surface morphology of g-C_3N_4, which was consistent with previously reported studies (Liu et al., 2020; Seng et al., 2020).

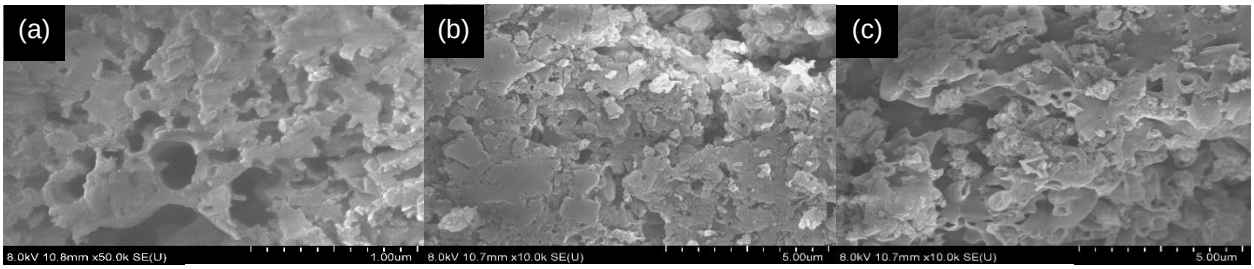

(d)

Photocatalyst	1-BCQD/CN		CQD/CN		CN	
Element (s)	Wt %	At%	Wt %	At %	Wt %	At %
C	40.65	43.54	35.18	38.86	32.70	36.31
N	50.20	46.10	62.82	59.48	64.21	61.12
O	1.36	1.10	2.00	1.66	3.09	2.58
B	7.78	9.26	N/A	N/A	N/A	N/A

Fig. 2 FESEM images of (a) CN, (b) CQD/CN and (c) 1-BCQD/CN, EDX and (d) EDX elemental analysis CN, CQD/CN and 1-BCQD/CN

EDX analysis was also conducted to investigate the elemental composition of each nanocomposite sample. Fig. 2(d) presents the EDX spectra of CN, CQD/CN and 1-BCQD/CN, respectively. It can be observed that both CN and CQD/CN contained C, N and O elements while 1-BCQD/CN showed the presence of an additional B peak, which validated the successful doping of B onto pristine CQDs. The presence of C in the EDX spectra could be due to the amorphous carbon of g-C_3N_4 nanosheets and co-catalyst CQDs. Meanwhile, the existence of N in the spectra could be ascribed to the construction of g-C_3N_4 using heptazine ($C_6H_3N_7$) as the fundamental building block of the graphitic carbon framework. Finally, the minor composition of O could be due to the formation of carboxyl groups (─COOH) during the synthesis of BCQDs as well as possible adsorption of water molecules on the photocatalyst surface.

Fig. 3(a)-(c) present the TEM images of CN, CQD/CN and 1-BCQD/CN. Similar to the FESEM image, the TEM image of CN depicted in Fig.3(a) features a highly porous 2D planar sheet with pores of estimated diameters ranging from 22 – 39 nm. Upon the incorporation of CQD and BCQD, no distinguishable changes were observed with regards to the surface morphology and structure of g-C_3N_4. The TEM images of CQD/CN and 1-BCQD/CN are depicted in Fig 3(b) and (c) respectively. Monodispersed quasi-spherical dark spots with an average diameter range of 6.076 and 6.024 nm (see Figure 3(d)) were observed on the CN sheets for CQD and 1-BCQD respectively. This indicated the successful formation of CQDs and BCQDs on the surface CN. The co-existence of BCQDs and CN with such close contact between them reaffired the successful preparation of the heterostructure nanocomposites. This unique 0D/2D layout is perceived to be beneficial for the effective transfer of photogenerated charge carriers, which will in turn lead to a reduction in electron-hole recombination rate.

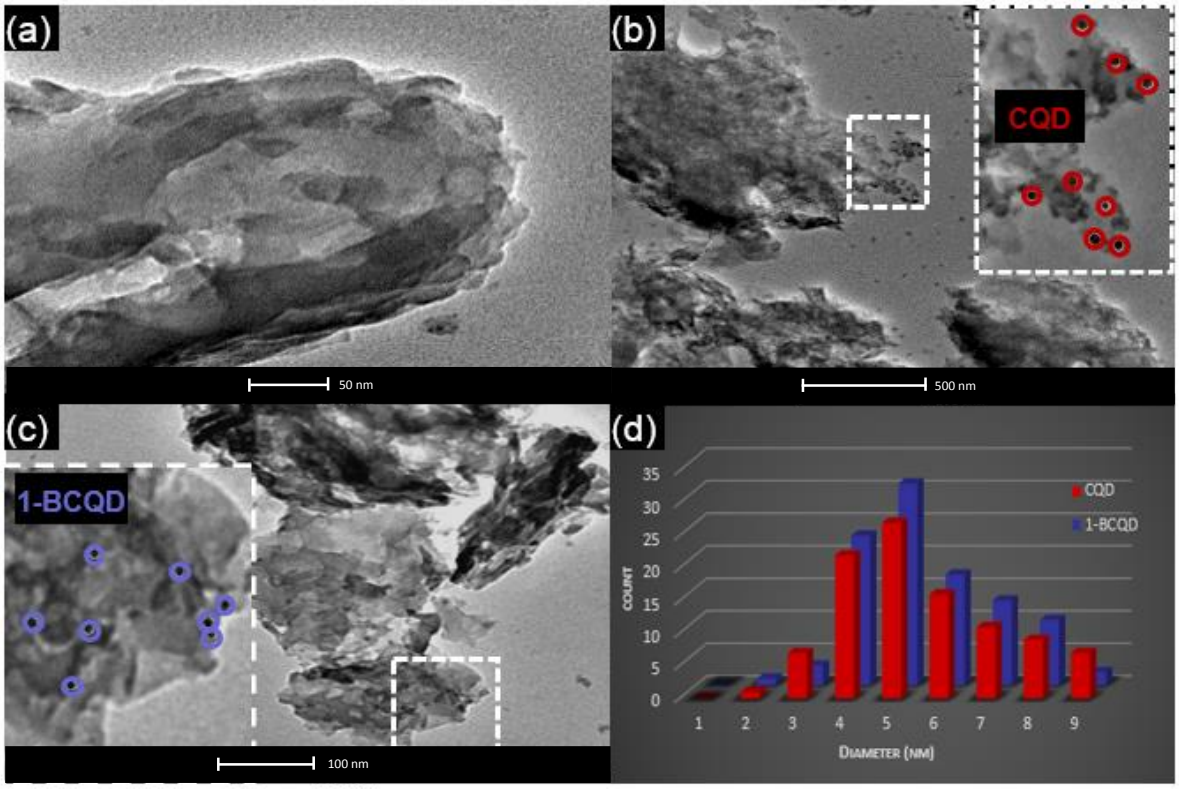

Fig. 3 TEM images of (a) CN, (b) CQD/CN and (c) 1-BCQD/CN; (d) particle size distribution of BCQD and CQD on 1-BCQD/CN and CQD/CN, respectively. Insets of Fig. 3(b) and 3(c) show enlarged figures of the areas enclosed in dashed boxes

The crystalline framework of CN, CQD/CN and 1-BCQD/CN were analyzed with XRD, a non-destructive test method for the identification of plane spacing and crystal structure based on monochromatic beam of X-rays. Fig. 4(a) presents the XRD patterns of CN, CQD/CN and 1-BCQD/CN. Two distinctive diffraction peaks were displayed by all the as-prepared photocatalytic samples, which validated the construction of stacked graphitic layers of g-C_3N_4 (JCPDS, No. 87-1526) (Ran et al., 2019; Orooji et al., 2020). The peak observed at a lower diffraction angle of 13.4° (d = 0.67 nm) corresponded to the (100) plane associated with the in-plane structural packing motif of heptazine units (Tyborski et al., 2013). On the other hand, a more-apparent peak located at approximately 27.4° (d = 0.325 nm) could be indexed to the (002) plane, corresponding to the typical interplanar stacking layers of conjugated aromatic compounds (Elshafie et al., 2020). It should be noted that all samples (CN, CQD/CN and 1-BCQD/CN) exhibited identical XRD trends. This indicated that the hybridization of CN with CQD or BCQD did not alter its fundamental crystalline layout, which was consistent with the microscopy images in Fig. 2 and 3. Interestingly, the characteristic peaks associated with CQD or BCQD were not observed in the XRD profiles. This may ascribe to the low quantity of quantum dots employed in the nanocomposite samples. Another possible reason for this observation could be the overshadowing of amorphous CQD by highly crystalline g-C_3N_4 polymers. Similar findings were also reported in several published work, where the hybridization of CQDs with different semiconducting materials (e.g. CQD/Fe_2O_3 and NCQD/TiO_2) were studied (Zhang et al., 2011; Martins et al., 2016). Fig. 4(b) shows the magnified XRD profiles of CN, CQD/CN and 1-BCQD/CN between 26 – 29°, where the (002) peaks were respectively located at 27.34°, 27.32° and 27.37° respectively. Generally, a slight right-shift in the

XRD peak is an implication of narrower interlayer and intralayer distances (Zhang et al., 2018). The full width at half maximum (FWHM) of the (002) peak was sequenced in an increasing order of CN, CQD/CN and 1-BCQD/CN, which indicated that 1-BCQD/CN possessed the greatest crystallite size in comparison with that of CN and CQD/CN.

The molecular structure and chemical composition of CN, CQD/CN and 1-BCQD/CN were also analyzed via FTIR as shown in Fig. 4(c). For CQD/CN and 1-BCQD/CN nanocomposites, the broad band at 3260 cm^{-1} was ascribed to the stretching of -OH groups with the presence of CQD and BCQD (Zhang et al., 2017b). Apart from that, there were no observable changes to the transmittance peaks of the samples. This once again affirmed the well-preserved chemical framework of CN with the coupling of CQD and BCQD. The sharp peaks located in the range of 1200 – 1650 cm^{-1} could be attributed to the stretching modes of -C-N heterocycles, displaying peaks located at 1646 cm^{-1}, 1578 cm^{-1}, 1411 cm^{-1}, 1329 cm^{-1}, and 1235 cm^{-1} (Kumru et al., 2019; Seng et al., 2020). On the other hand, the peak at 1081 cm^{-1} could be associated to the oxygenated functional group C-O (Wang et al., 2017b). The typical breathing mode of tri-s-triazine unit of g-C_3N_4 homojunction was represented by the intense peak at 808 cm^{-1} (Zhang et al., 2020a).

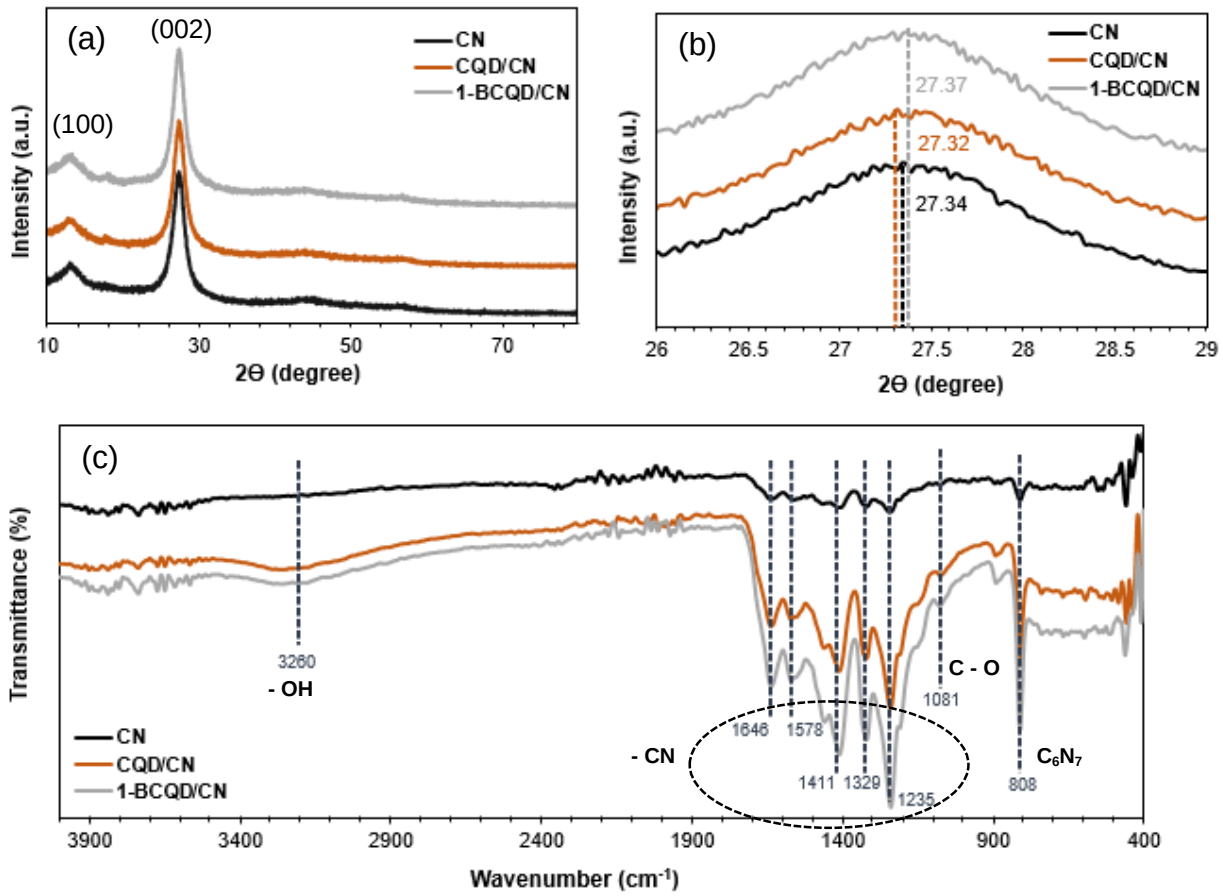

Fig. 4 (a) XRD spectra, (b) Magnified (002) peak of the XRD profile and (c) FTIR spectra of CN, CQD/CN and 1-BCQD/CN

To gain a deeper understanding of the chemical interactions, XPS analysis was carried out to identify the elemental composition and bonding on the surface of the photocatalysts. As shown in Fig. 5(a), the survey spectra of CN, CQD/CN and 1-BCQD/CN show that the samples were primarily composed of C, N and O. The atomic concentrations and weight percentages of each element are summarized in Fig. 5(e). Intriguingly, the B element was not detected in the 1-BCQD/CN sample, which could be due to the low quantity of dopant used on the hybrid nanocomposite. Nevertheless, the successful integration of the B dopant was verified through EDX analysis as discussed earlier (see Fig 2(f)). Fig. 5(b) presents the deconvoluted C 1s spectra of 1-

BCQD/CN, where four prominent peaks at 288.85, 288.15, 285.70 and 284.72 eV were observed. These peaks corresponded to the C-N-C bonds, sp^2-hybridized atomic carbon in N-C=N of the aromatic systems, C-O/C=O and C-C/C=C coordination, respectively (Liu et al., 2011; Qiao et al., 2015; Tan et al., 2015; Qin and Zeng, 2017). Besides that, the N 1s core level spectrum as depicted in Fig. 5(c) displayed a dominant peak centered at 398.57 eV, which could be associated to the pyridine N atom of the s-triazine rings (Sun et al., 2015; Cao et al., 2018). The N peak at 399.64 eV could be attributed to the pyrrolic N atom as part of the π-bonding system while the peak at 400.95 eV was ascribable to the graphitic N atom bonded to three carbon atoms within the aromatic rings (Kundu et al., 2010; Qiao et al., 2015; Fontelles-Carceller et al., 2016). The O 1s spectra, as shown in Fig. 5(d) was deconvoluted to two fitted peaks: 533.09 eV and 531.71 eV, which corresponded to -OH and C-O/C=O bonds respectively. These represented the oxygenic components of the B-doped CQDs which was similarly reported in literature (Qin and Zeng, 2017; Kesarla et al., 2019).

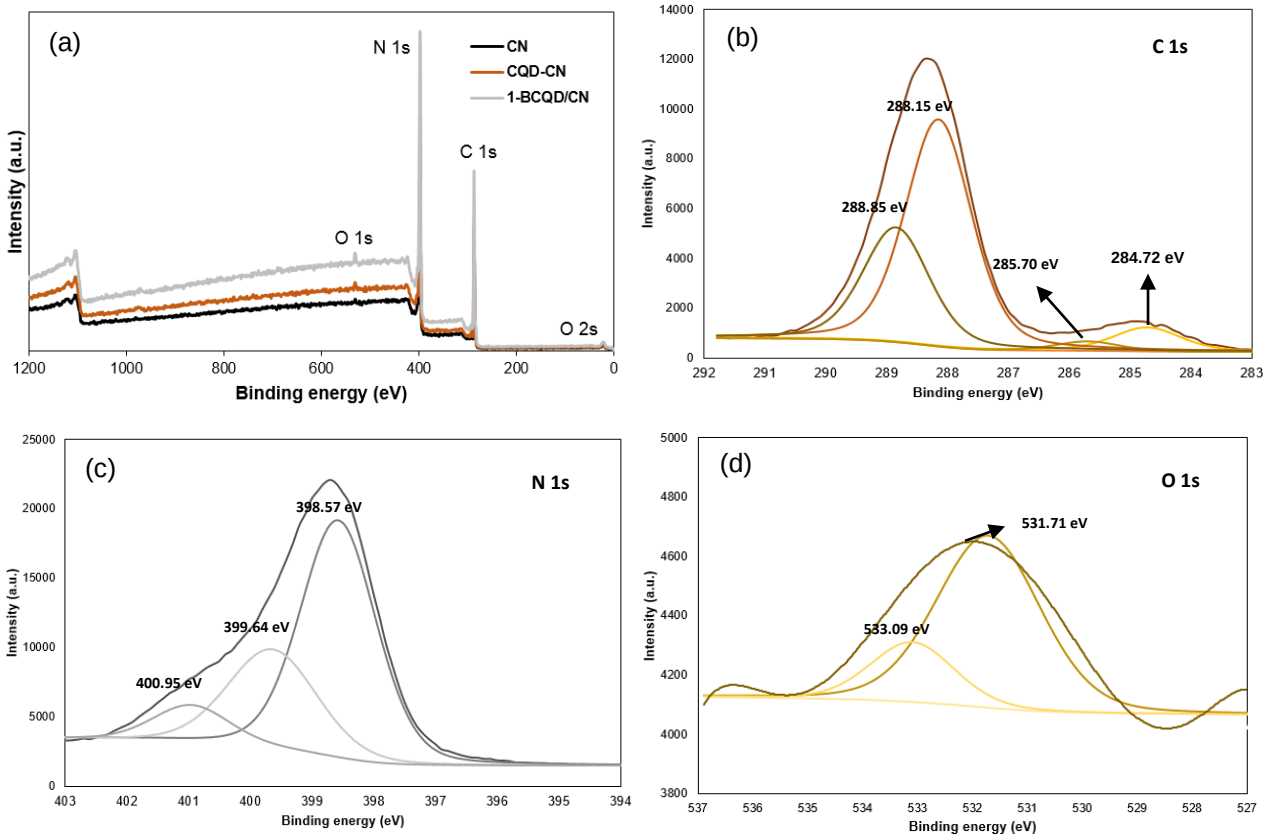

(e)

Photocatalyst sample	Atomic percentage (At %)			Weight percentage (Wt %)		
	C 1s	N 1s	O 1s	C 1s	N 1s	O 1s
CN	38.67	59.90	1.43	35.02	63.26	1.72
CQD/CN	40.19	59.11	0.70	36.52	62.63	0.85
1-BCQD/CN	40.44	58.04	1.52	36.71	61.44	1.85

Fig. 5 (a) XPS Survey spectra of CN, CQD/CN and 1-BCQD/CN (b) C 1s spectra, (c) N 1s spectra, (d) O 1s spectra of 1-BCQD/CN and (e) Tabulated data of each element for CN, CQD/CN and 1-BCQD/CN

The optical properties of the as-developed photocatalysts were studied using UV-Vis DRS. As presented in Fig. 6(a), the adsorption bands of CN, CQD/CN and 1-BCQD/CN were categorized under the violet-blue regime of the visible spectrum. As observed from Fig. 6(a), the samples presented similar optical absorbances with absorption edges of CN, CQD/CN and 1-BCQD/CN at *ca.* 460, 453 and 452 nm respectively. As the changes in the absorption edge of bulk

and CQDs-based CN was relatively insignificant, it is reasonable to infer that CQDs primarily served as electron transfer conduits to enhance the transportation of photoinduced charge carriers (Seng et al., 2020). The measurements obtained were similar to the typical optical absorption of g-C_3N_4 published in the previous studies (Liu et al., 2011; Yan et al., 2020).

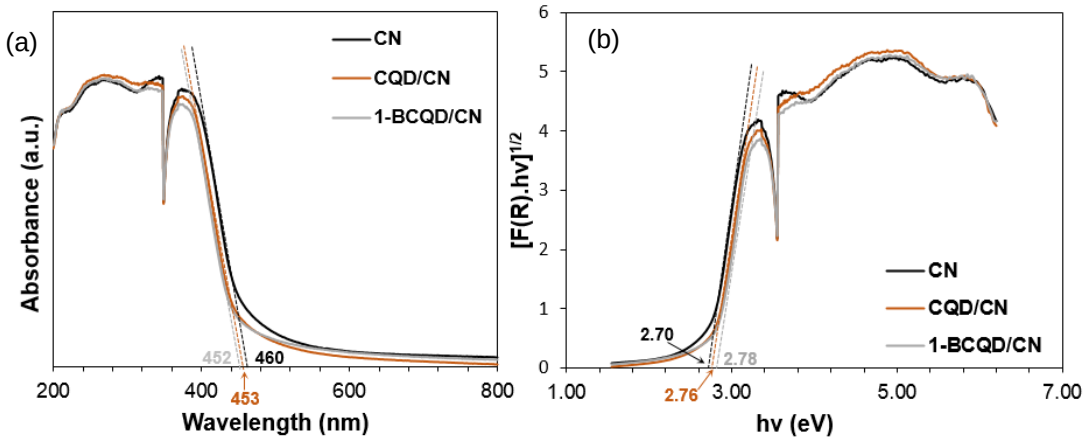

Fig. 6 (a) UV-Vis diffuse reflectance spectra and (b) Corresponding Tauc plot of CN, CQD/CN and 1-BCQD/CN

The optical band gap energy (E_g) of a semiconductor is defined as the energy difference between the highest occupied state in the VB and the lowest unoccupied state in the CB. The E_g can be determined via the construction of a Tauc plot i.e., a graph of $[F(R).hv]^n$ vs. photon energy (hv) (Viezbicke et al., 2015). The absorption coefficient, Planck constant and optical frequency are denoted as F(R), h and v respectively whereas the value of exponent n depends on the transition nature of the material (Xu and Gao, 2012; Kumar et al., 2017). As presented in Fig 6(b), the E_g values of CN, CQD/CN and 1-BCQD/CN were approximately 2.70, 2.76 and 2.78 eV respectively. The widening of E_g upon CQD or BCQD doping could be ascribed to the quantum size effect as well as the presence of structural defects in the hybrid nanocomposites (Liu et al., 2007; Klubnuan et al., 2016).

3.2 Evaluation of photocatalytic activity

The photocatalytic activities of CN, CQD/CN and BCQD/CN (with varying mass loadings of the B dopant) were assessed via the photodegradation of organic dye RhB. Prior to light illumination, the suspension of photocatalyst and dye solution was stirred for 30 min without light to establish an adsorption-desorption equilibrium. The almost-complete saturation at the solid-liquid interface minimizes the effect of physical interaction on the changes in RhB concentration as photocatalytic reaction occurs (Zhang et al., 2016a). The photocatalytic experiments were carried out under the irradiation of an 18 W LED light for a total duration of 4 hrs. The primary objectives of this study are: (i) to analyze the effect of incorporating B-dopant on CQDs-decorated n/n junctioned g-C_3N_4; and (ii) to investigate the optimum mass loading of B on the hybrid sample. Control experiments were also conducted following the procedures outlined in Section 2.4, but without (i) the photocatalyst sample; and (ii) light source (see Supplementary Information – Section 1.0). In both conditions, no significant discoloration of RhB was observed, which confirmed the indispensable roles of the photocatalyst and excitation source for the photodegradation process. Fig. 7(a) shows the graph of ln (C_0/C) against irradiation time of each photocatalyst sample for the evaluation of the k value according to the Langmuir-Hinshelwood model. The best-fitted lines signified the linear relationship between ln (C_0/C) and irradiation time, thereby confirming that the photocatalytic degradation of RhB dye was in accord with the first-order kinetics.

Fig. 7(b) depicts an overview of the photodegradation efficiencies and kinetic rate constants of CN, CQD/CN and BCQD/CN with varying mass loadings of B (0.5-BCQD/CN, 1-BCQD/CN, 2-BCQD/CN and 3-BCQD/CN). As observed, the photocatalytic performances were in the order of: 1-BCQD/CN > 2-BCQD/CN > 3-BCQD/CN > 0.5-BCQD/CN > CQD/CN > CN. In comparison to pure CN and CQD/CN, all B-modified CQD/CN photocatalysts displayed a

pronounced improvement in photoactivities. The optimum 1-BCQD/CN sample achieved a remarkable 96.8% removal of RhB dye in 4 hrs under LED light illumination with an associated k value of 1.39×10^{-2} min^{-1}. This translated to an improvement factor of 3.6 and 2.8 over pure CN and CQD/CN, which validated the significance of heteroatom B doping on CQDs for photocatalytic activity enhancement. The discoloration process of RhB in the presence of 1-BCQD/CN is shown in inset of Fig. 7(d). Interestingly, the color of the organic dye was observed to change progressively from its characteristic pink shade to orange and yellow, before turning colourless eventually.

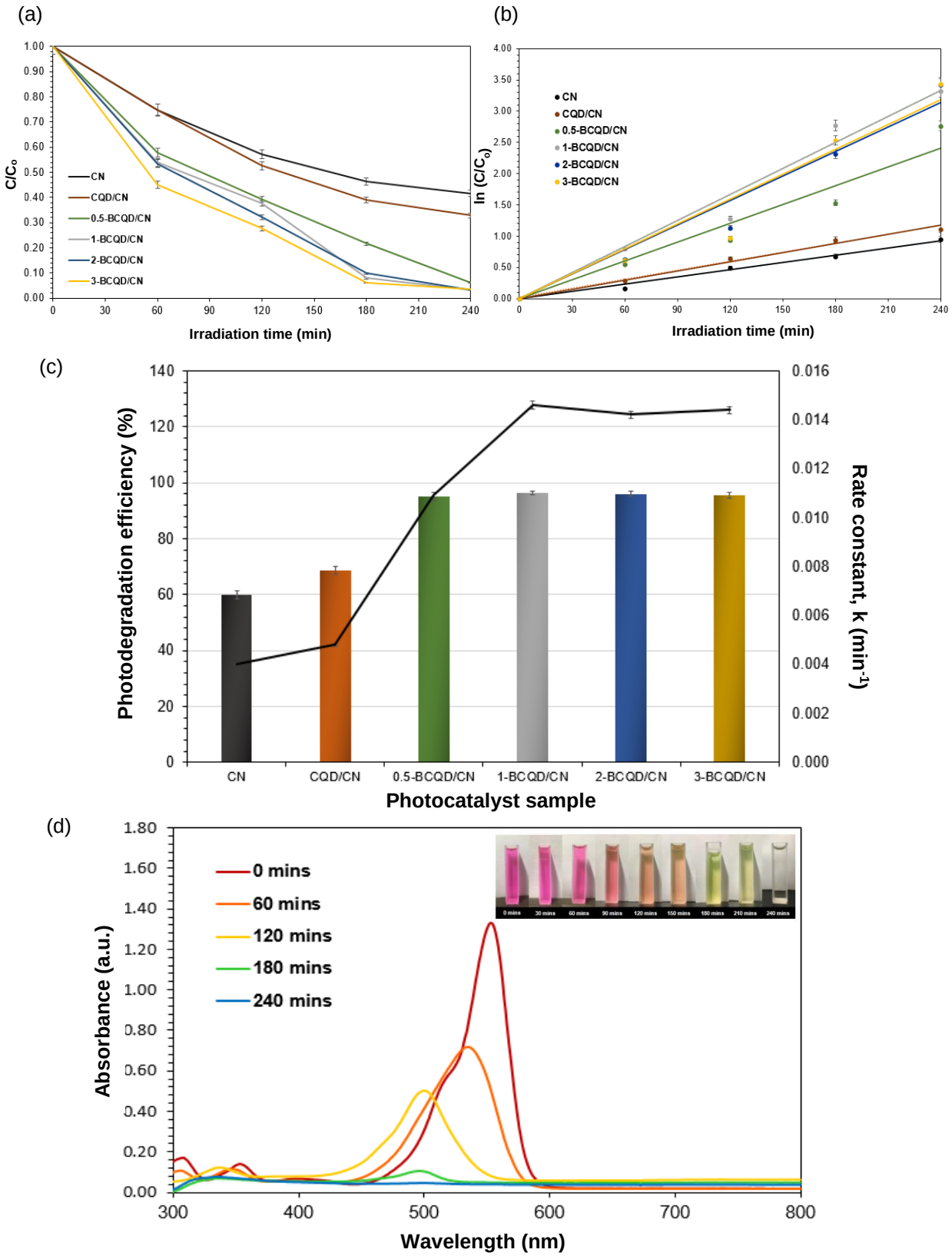
(a)
C/C$_o$
Irradiation time (min)
CN
CQD/CN
0.5-BCQD/CN
1-BCQD/CN
2-BCQD/CN
3-BCQD/CN
(b)
ln (C/C$_o$)
Irradiation time (min)
(c)
Photodegradation efficiency (%)
Rate constant, k (min^{-1})
Photocatalyst sample
(d)
Absorbance (a.u.)
Wavelength (nm)
0 mins
60 mins
120 mins
180 mins
240 mins

445 `

Fig. 7 (a) RhB degradation profile with respect to time, b) Linear graph of ln (C_o/C) against irradiation time for all photocatalyst samples, (c) RhB degradation efficiency and kinetic rate constant of each photocatalyst under the irradiation of LED light and (d) Absorbance curves of 1-BCQD/CN at wavelengths between 300 and 800 nm for 240 mins with 60 min intervals (Inset: gradual decolorization of the RhB dye as a result of photodegradation in the presence of 1-BCQD/CN)

As demonstrated in Fig. 7(b), the mass loading of B on CQD/CN did not impose prominent effects on the photodegradation efficiency of the hybrid material. However, its profound impact on the apparent rate constant was evident. Based on Fig. 7(b), the evaluated rate constant demonstrated an appreciable surge from 1.09×10^{-2} min^{-1} (0.5-BCQD/CN) to 1.46×10^{-2} min^{-1} (1-BCQD/CN). This observation highlighted the significance of precise mass loading of the B-dopant on CQD/CN in terms of expediting interfacial charge transfer and hindering electron-hole recombination. Fig. 7(c) shows the absorbance trend exhibited by the RhB solution catalyzed over 1-BCQD/CN sample under visible light irradiation. For a RhB dye, the characteristic peak of the absorbance curve was noted at a wavelength of 554 nm prior to photodegradation. Apart from the gradual decrease in absorbance intensity with time, the peaks shifted gradually towards the blue region (left) of the visible spectrum as the illumination time lengthened. This was in congruent with the reported studies on the photodegradation of RhB catalyzed by g-C_3N_4/g-C_3N_4 homojunction systems, Ag_3PO_4 nanoparticles and Ag_3VO_4/β-Ag_3VO_4 nanocomposites (Gao et al., 2017; Xu et al., 2017; Phang et al., 2020a). Besides, the left-shifted peaks signified the generation of de-ethylated intermediates as the chromophores and aromatic rings of the RhB dye undergone deconstruction (Li et al., 2008; Chiu et al., 2019).

In comparison with several previously published studies, the optimum photocatalytic nanocomposite sample 1-BCQD/CN performed fairly well among its counterparts. Table S1 in Supplementary Information- Section 2.0 presents the photodegradation performance of different

photocatalytic nanocomposites as reported in literature (da Silva et al., 2014; da Silva et al., 2016; Liu et al., 2017; Muraro et al., 2020; Sahu et al., 2020; Zhu and Zhou, 2020; da Silva et al., 2021).

3.3 Photoelectrochemical and PL analysis

To further study the charge migration behavior and separation of photo-generated electron-hole pairs across the interface of BCQD/CN photocatalyst, transient photocurrent response and Mott-Schottky plots were also constructed. As presented in Fig. 8(a), the transient photocurrent measured were plotted with respect to time for CN, CQ/CN and 1-BCQD/CN with alternate cycles of on-off visible light irradiation to study their photoelectronic properties. The electric current generated by the photo-excited charge carriers were measured via transient photocurrent as the visible light pulse was turned on and decayed promptly with the light shut off (Xiang et al., 2011; Phang et al., 2020a). It is observed that there was a significant improvement in the transient photocurrent response exhibited by 1-BCQD/CN. The relatively high current density of 1-BCQD/CN is an implication of the boosted effectiveness in electron-hole pairs separation which may be ascribed to the presence of BCQDs. The doping of BCQDs on CN played a significant role as the channels for electron transport (as discussed previously in Section 3.2) and this inference was further supported by the generally low Fermi level of CQDs (-0.3 eV) relative to that of CN (-0.61 eV) (Tian et al., 2017; Wang et al., 2017a). Thus, the photoinduced electrons were prompted to shuttle from CN to BCQDs, in which the BCQDs served as electron traps, to effectively retard the recombination of electron-hole pairs (Wang et al., 2018; Di et al., 2020).

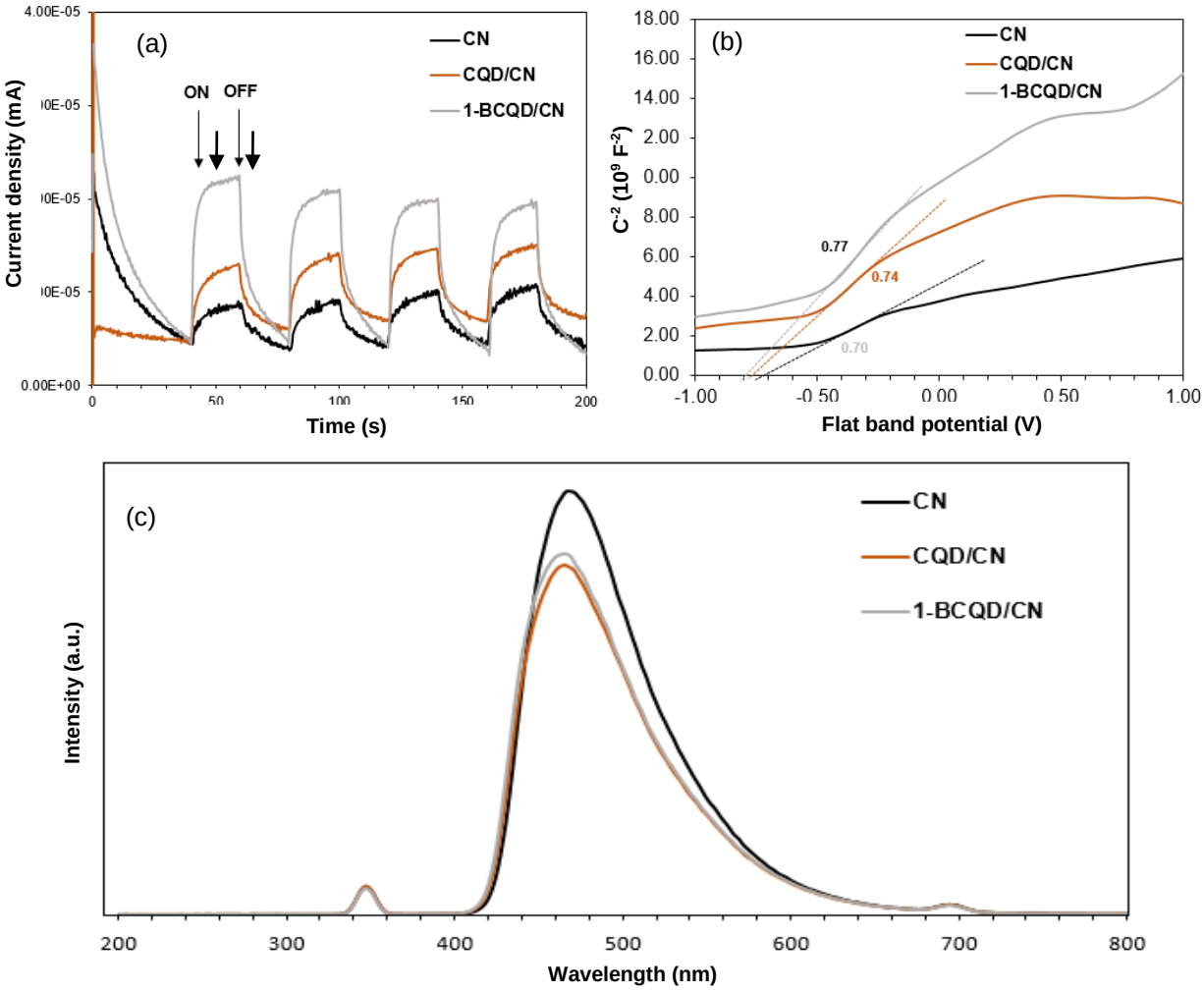

489

490 **Fig. 8** (a) Transient photocurrent response, (b) Mott-Schottky plots and (c) PL spectra of CN, CQD/CN and 1-
491 BCQD/CN

492 Moreover, Mott-Schottky analysis were performed as an effort to analyze the interrelation
493 between applied potential and capacitance space charge region. Fig 8(b) presents the Mott-
494 Schottky plots of the photocatalyst samples and the flat band potential (E_{fb}) was evaluated via the
495 extrapolation of tangent lines at the x-axis intercept whereby $C^{-2} = 0$. From the Mott-Schottky plot,
496 the E_{fb} of CN, CQD/CN and 1-BCQD/CN were determined as -0.70, -0.74 and -0.77 V vs.
497 Ag/AgCl respectively. The E_{fb} was marginally lowered with the incorporation of CQD and BCQD,
498 indicating a depletion in photo-generated holes on the surface of the hybrid photocatalysts

499 (Rangaraju et al., 2009; Liu et al., 2014). On top of that, Mott-Schottky plots of the samples
500 displayed positive slopes which is the typical characteristic of an n-type semiconductor (Guan et
501 al., 2020). Hence, this verified the successful construction of photocatalytic nanocomposites
502 featuring n/n homojunction via coupling of g-C_3N_4 derived from urea and thiourea. The measured
503 flat band potentials are with respect to NHE) using the conversion equation as expressed in
504 Equation (3) whereby pH value was approximately 7.0 and E_{AgCl} = 0.197 V at ambient temperature
505 (Babu et al., 2018; Li et al., 2020a):

$$E_{fb}(vs.NHE) = E_{fb}(vs.Ag/AgCl) + E_{(AgCl)} + 0.059pH \quad (4)$$

506 Upon conversion, the E_{fb} (vs. NHE) of CN, CQD/CN and 1-BCQD/CN were evaluated as -0.09, -
507 0.13 and -0.16 V respectively. It is well-entrenched that the E_{cb} of an n-type semiconductor is
508 generally 0.1-0.3 V more negative than its E_{fb}, as governed by the electron effective mass and
509 carrier concentration (Tian et al., 2015). In this case, the difference in voltage between E_{fb} and E_{cb}
510 was set at 0.3 V. Therefore, the E_{cb} were calculated as -0.39, -0.43 and -0.46 V for CN, CQD/CN
511 and 1-BCQD/CN respectively. Subsequently, the valence band potential, E_{vb} were evaluated
512 according to the equation as follows:

$$E_{vb} = E_{cb} + E_g \quad (5)$$

513 The E_{vb} of CN, CQD/CN and 1-BCQD/CN were obtained as 2.31, 2.33 and 2.32 V respectively.

514 The PL spectra exhibited by CN, CQD/CN and 1-BCQD/CN were also presented in Fig
515 8(c). Hitherto, the governing factor of PL mechanism has yet to be thoroughly elucidated and
516 remains highly debatable as there are multiple argumentations regarding this subject matter. The
517 proposed concepts include quantum confinement effect, functional groups, structural defect,
518 surface passivation and functionalization, etc (Wang et al., 2014; Choi et al., 2016; Das et al.,
519 2017). Nonetheless, it has been widely perceived that the intensity of PL emission is closely

associated with the recombination of photo-excited charge carriers. Thus, PL spectra are commonly utilized to interpret the migration behavior, separation and transfer mechanism of electron-hole pairs (Zhu et al., 2019). Based on Fig. 8(c), the PL emission spectra of CN, CQD/CN and 1-BCQD/CN featured a prominent luminescence peak ranging from 420-520 nm. As it is well known, intense fluorescence (FL) emission implies a high rate of electron-hole recombination, whereby photogenerated holes from the lower energy states and electrons from the higher energy states recombine to release energy in the form of light (Wang et al., 2020). It is observed from Fig. 8(c) that CN exhibited the strongest PL emission spectra. On the contrary, relatively low PL emission peaks were demonstrated by CQD/CN and 1-BCQD/CN, reflecting the suppressed electron-hole recombination in the presence of pristine or B-doped CQDs. This also reaffirmed the role of CQDs in the hybridized photocatalytic nanocomposites as an electron transport conduit, considerably boosting the effectiveness of charge carrier transport and separation. Fundamentally, a low charge carriers recombination rate is highly beneficial towards the photocatalytic efficiency of a semiconductor nanomaterial.

3.7 Free radical scavenging test and plausible photocatalytic charge transfer mechanism

A series of scavenging tests were performed to identify the role of each reactive species in the photocatalytic mineralization of RhB and to propose a plausible photocatalytic mechanism over BCQD/CN. The declined photocatalytic performance in the presence of each scavenger implied the importance of the associated reactive species. The scavenging chemicals, TEOA, BZQ and IPA were applied to capture the relevant reactive species, h^+, $\cdot O_2^-$ and ·OH respectively. The changes in concentration of RhB and degradation efficiency of BCQD-CN are summarized in Fig. 9(a). As observed in Fig. 9(b), it is evident that there was a drastic decrease in photoactivity upon the addition of TEOA (scavenger of h^+), indicating that h^+ species were indispensable for RhB

photodegradation. Precisely, h^+ reactive species held a crucial role in the generation of radicals including ·OH and OH^-, which actively took part in the mineralization of RhB ions (RhB^+) into photodegraded products. In the absence of h^+ species, the generation of ·OH radicals is not viable as the oxidation potential of water (H_2O/·OH = +2.73 eV) is more positive than the VB potential of the photocatalyst sample (Wang et al., 2017a). Nevertheless, ·OH radicals could also be generated via a different pathway whereby the reduction of elementary oxygen leads to the formation of $\cdot O_2^-$ species, which are then further reduced to ·OH radicals through multiple-electron reduction reactions. In addition, the VB potential of BCQD/CN was more positive than the standard redox potential of waterborne hydroxyl radicals (·OH/OH^- = +1.99 eV), rendering the oxidation of OH^- feasible (Wu et al., 2015). In short, these reactive species are crucial in the degradation and mineralization of RhB^+ under light irradiation.

(a)

Scavenger	Reactive species	C/C_o at t = 240 mins	Degradation efficiency (%)
TEOA	h^+	0.808	19.16
BZQ	$\cdot O_2^-$	0.773	22.74
IPA	·OH	0.178	82.17
Without	N/A	0.032	96.77

(b)

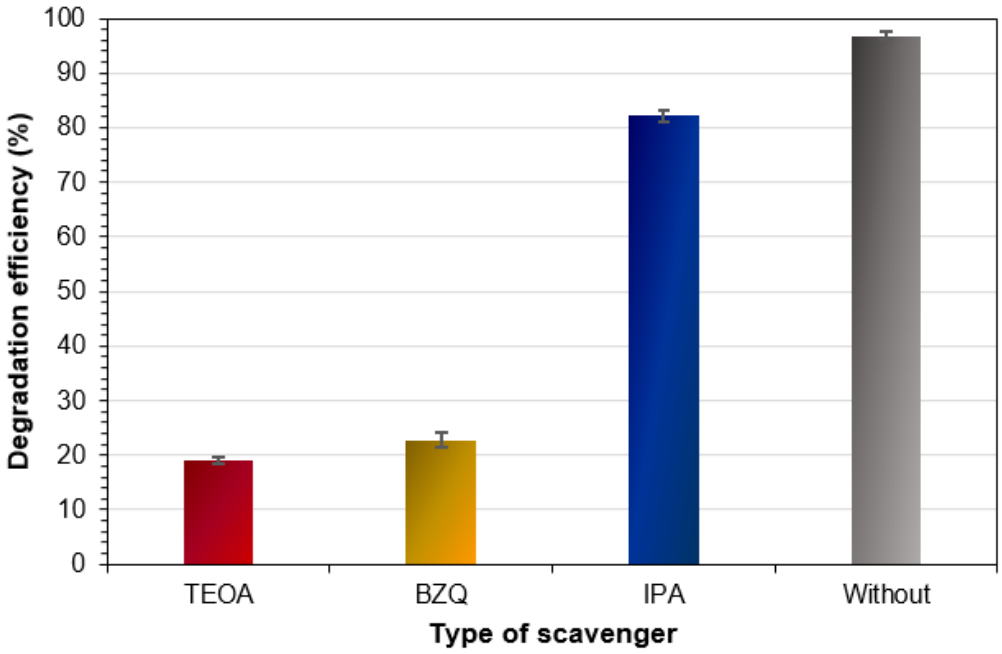

554

555 **Fig. 9** (a) Summary of photocatalytic performance and (b) Graph of photodegradation efficiency displayed by 1-
556 BCQD/CN in the presence of different scavengers

557 Based on the scavenging test, a plausible step-by-step charge transfer mechanism for RhB
558 photodegradation is presented in Fig. 10. The entire photo-reaction is initiated by the irradiation
559 of visible light, where the electrons from VB are excited and directed towards CB. Upon the
560 departure of electrons, holes are generated at the VB concurrently. Due to the difference in CB
561 and VB levels of g-C_3N_4 homojunction derived from urea and thiourea, the photo-generated
562 electrons and holes are separated more effectively in comparison to the charge transfer within a
563 pristine g-C_3N_4 (Liu et al., 2018). Specifically, the flow of photogenerated electrons (e^-) is directed

564 from the higher CB level of thiourea to that of urea while majority of the photogenerated holes (h^+)
565 are prompted to flow from the lower VB level of urea to that of thiourea. The opposite direction
566 in flow of charge carriers minimizes the recombination possibility for electrons and holes.
567 Furthermore, the doping of CQDs with heteroatoms B enriched the presence of structural defects
568 on the functionalized surface of BCQDs, effectively trapping more photo-excited charge carriers
569 and hampered the recombination of electrons and holes (Peng et al., 2020). Consequently, the
570 photoinduced electrons from VB of CN are readily transferred to the BCQDs due to their lower
571 energy levels (Wang et al., 2017a). The electrons are also captured and accumulated in the BCQDs
572 attributed to their excellent conductivity and large capacity for electron storage (Ong et al., 2017).
573 The electrons accumulated in the BCQDs and remnant of electrons in CN are primarily responsible
574 for the reduction of O_2 to generate superoxide anion radicals ($\cdot O_2^-$). The reduction process is
575 feasible as the CB levels of the nanocomposite is more negative than the redox potential of $O_2/\cdot O_2^-$
576 at -0.16 V (Krumova and Cosa, 2016). The $\cdot O_2^-$ radicals are indispensable for the mineralization
577 of RhB dye as evidenced by the scavenging test. On the other hand, the photoinduced holes in VB
578 are gradually transported to the surface and participate in the oxidation process of hydroxyl species
579 into hydroxyl radicals (·OH) as the VB level of BCQD/CN is more positive as compared to the
580 redox potential of $OH^-/\cdot OH$ at +1.89 V (Armstrong et al., 2015). It is also worth mentioning that
581 the change in redox potential ability upon hybridization is negligible as ratiocinated from the
582 evaluated VB and CB energy levels of pristine CN, CQD- and BCQD-based CN. Therefore, it is
583 reasonable to deduce that the BCQD and/or CQD mainly acted as channels to facilitate electron
584 transport and storage for the photocatalytic enhancement. Another factor that should be taken into
585 consideration for RhB photodegradation is the challenge of possible colloidal instability,
586 competition over active sites and susceptible hole scavenging posed by the inorganic chloride

anions (Cl^-) (Chong et al., 2010). Nonetheless, the presence of π-π interactions on the exterior of the nanocomposite photocatalyst enhanced the adsorption of organic pollutants, resulting in a boosted photocatalytic efficiency. Ultimately, the mineralization process of RhB pollutants was expedited by reactive species including ·OH, $\cdot O_2^-$ and h^+ in the formation of photo-degraded products.

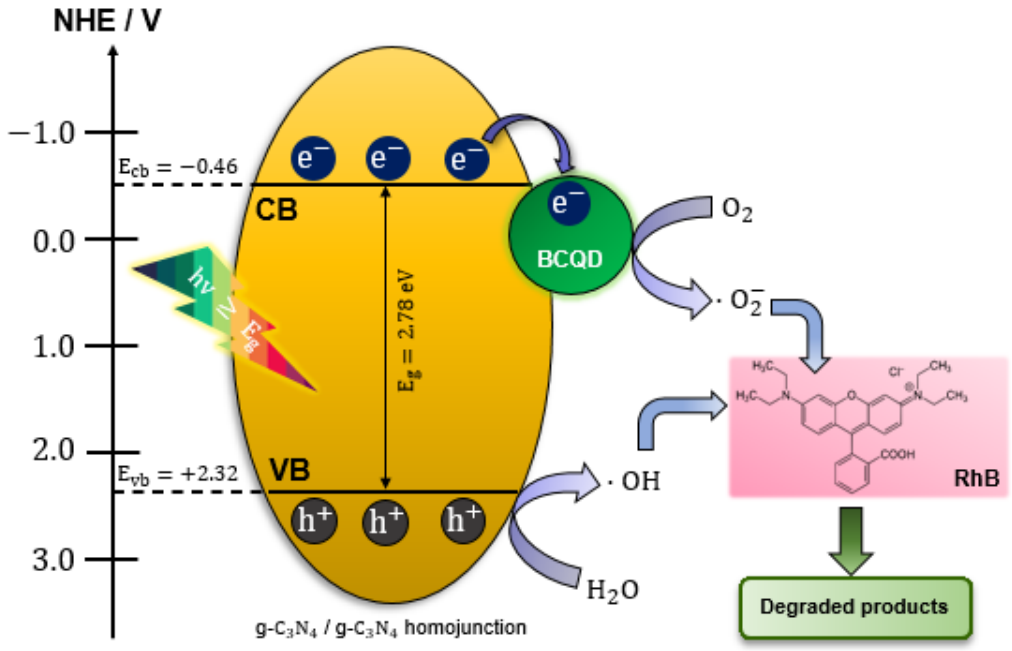

Fig. 10 Schematic illustration of the plausible photocatalytic mechanism and a series of photo-reaction chain for RhB dye degradation in the presence of CQD-based g-C_3N_4 as photocatalyst

3.8 Recyclability test

In addition to the initial photocatalytic performance, the reusability of photocatalysts is also critical for practical and long-term applications. For the evaluation of its photo-stability, the optimal sample, 1-BCQD/CN was assessed and recycled for 3 consecutive cycles under identical conditions. The photocatalyst sample was separated from the dye solution via vacuum filtration and washed copiously with distilled water prior to oven-drying for the subsequent cycle. To

account for the weight loss in the recovered photocatalyst sample, the amount lost was compensated by a decreased volume of dye solution following a fixed ratio of 0.15 g photocatalyst to 100 mL RhB solution (10 mg/L). The recyclability test of 1-BCQD/CN is presented in Fig. 11(a). It is apparent that the photoactivity of 1-BCQD/CN was successfully retained even after 3 successive cycles without any observable regression in its photocatalytic performance. Precisely, the 1-BCQD/CN photocatalyst sample maintained 98.6 % of its original activity after 3 consecutive runs. Furthermore, there were no significant changes to the molecular structure and chemical composition of the recycled 1-BCQD/CN with reference to its fresh counterpart as evidenced by their respective FTIR spectra presented in Fig. 11(b). This suggests that 1-BCQD/CN is superior in term of its stability and durability, which are highly advantageous from the economic and sustainability perspectives for probable industrial applications in the future.

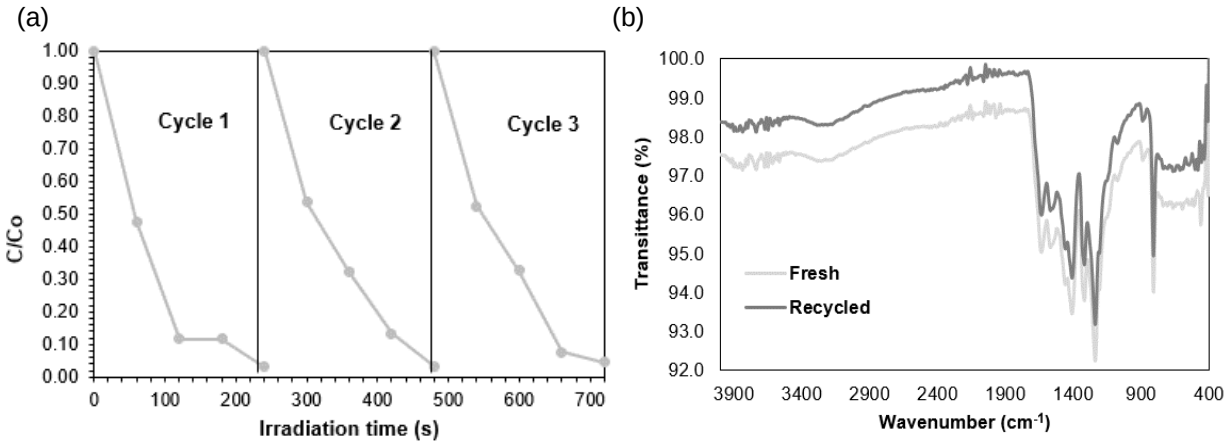

Fig. 11 (a) Recyclability test of 1-BCQD/CN for 3 consecutive cycles and (b) FTIR spectra of 1-BCQD/CN in fresh and recycled conditions

615 **3.9 Process optimization of RhB photodegradation underlying 1-BCQD/CN**

616 Regression analysis was performed and a second-order polynomial equation was determined that
617 best demonstrates the empirical relationship between photodegradation efficiency of RhB and the
618 independent variables:

$$RhB\ degradation\ (\%) = 124.6 - 26.53x_1 - 1.680x_2 + 456.3x_3 \quad (6)$$
$$+1.2596x_1^2 + 0.2256x_1x_2 - 16.26x_1x_3 - 9.73x_2x_3$$

619 Based on equation 6, the pH value and initial dye concentration had negative effects on the
620 response (RhB degradation), whereby the photoactivity increases as the pH and initial RhB
621 concentration decrease. On the other hand, dosage of photocatalyst had a positive effect on the
622 photodegradation process as a higher rate of RhB removal was observed with an increase in the
623 photocatalyst amount. Table 2 presents the model summary of regression equation for
624 photocatalytic degradation of RhB. From the results displayed in Table 2, the coefficient of
625 determination (R^2) calculated is close to 1 and the adjusted value is also comparable to the
626 corresponding R^2, which indicates the adequacy of the regression model. Furthermore, the
627 relatively low prediction error sum of squares (PRESS) reflected in a high predicted R^2.

628 Table 2. Model summary for the regression model

Standard deviation	R^2	R^2 (Adjusted)	PRESS	R^2 (Predicted)
2.5528	99.56 %	99.12 %	309.996	97.01 %

629 PRESS: Prediction error sum of squares

630 Based on the analysis of variance (ANOVA) results, it is further verified that the regression
631 model is a good fit to the experimental data as p-values of all coefficients are less than 0.05. The
632 analysis results also showed that all three independent variables are influential to the removal of
633 RhB to a certain degree, with pH value, initial concentration and photocatalyst dosage contributing
634 57.49, 18.77 and 4.23 % to the overall RhB photodegradation process respectively. The model was

further validated by comparing the experimental and predicted responses for each run, it was observed that the difference between these values is marginal as tabulated in Table 3. On top of that, Fig.12 (a) shows that the predicted values are linearly proportional to that of experimental with slight deviation.

Table 3. The set independent variables, experimental and predicted data for RhB degradation

Run order	Independent variables			Degradation of RhB (%)	
	x_1	x_2	x_3	Experimental	Predicted
1	11	20	0.10	6.866	9.498
2	11	20	0.20	17.544	17.782
3	7	30	0.10	4.373	2.644
4	3	30	0.15	41.903	43.593
5	7	20	0.15	22.054	20.776
6	3	20	0.10	56.646	57.574
7	7	10	0.10	22.892	24.120
8	11	10	0.15	23.132	20.219
9	7	30	0.20	7.073	7.702
10	11	30	0.15	7.036	7.061
11	3	10	0.15	94.102	92.847
12	7	10	0.20	45.043	48.638
13	3	20	0.20	80.330	78.866

3.9.1 Effect of pH value

The solution pH is one of the primary factors that affect the process of RhB photodegradation and pH value of effluents differ considerably across various industrial sectors (Ghosh and Pal, 2020). Herein, the pH value of RhB solution was varied from 3 to 11 and it was observed that 1-BCQD/CN displayed relatively high degradation effectiveness in the acidic environment as compared to the alkaline region. It is well known that RhB dye has an acid dissociation constant, pKa of approximately 3.1 (Huy et al., 2017; Tho et al., 2018). In the case of pH > pKa, the carboxyl

groups of RhB are deprotonated with the formation of negatively charged ions. In conjunction with the study of pH value effect on RhB photodegradation performance of the optimum photocatalyst, the pH_{pzc} of 1-BCQD/CN was also evaluated. Based on the pH drift method, the pH_{pzc} of 1-BCQD/CN was determined as 7.0 (Fig. 12 (b)). This implied that the surface of the photocatalyst is positively charged when the pH of the solution is less than pH_{pzc} and vice versa (Yang et al., 2020b). The value of pH_{pzc} evaluated is comparable to several other g-C_3N_4-based semiconductors as reported previously (Zhang et al., 2014; Fronczak et al., 2018). Therefore, the dye adsorption on 1-BCD/CN was enhanced due to its positively charged surface being in contact with deprotonated RhB ions. In contrast, the drastic decline in the photodegradation of RhB as pH value increases may be ascribed to the zwiterionic form of RhB whereby the carboxyl and xanthene groups of RhB monomers combine to form dimers, impeding the contact between RhB and 1-BCQD/CN (Huy et al., 2017). Nevertheless, the correlation between pH value, pKa and pH_{pzc} is not the sole governing factor that determine the RhB photodegradation efficiency, there are other influences such as hydrogen bonding and hydrophobic interactions (Dahri et al., 2016; Kooh et al., 2016; Madjene et al., 2021).

3.9.2 Effect of photocatalyst dosage

The rate of RhB photocatalytic degradation is strongly dependent on the amount of photocatalyst involved. The dosage of the photocatalyst 1-BCQD/CN was varied from 0.10 to 0.20 g. It was observed that the percentage of RhB photodegradation was improved with increasing dosage of photocatalyst, this is attributed to the growing number of photogenerated electron-hole pairs and availability of active sites (Ramanathan et al., 2019; Saher et al., 2021).

3.9.3 Effect of initial RhB concentration

Another influential factor on the photocatalyst degradation of RhB is the initial dye concentration, which was studied by varying the initial concentration of RhB from 10 to 30 mg/L. Based on the optimization results, it can be deduced that the rate of RhB photodegradation decreased with an increase in initial RhB concentration. The drop in RhB photodegradation performance with relatively high concentration is mainly due to the limited amount of light penetration through the dye solution. Besides that, the large amount of dye molecules that were absorbed onto the surface of the photocatalyst may obscure the active sites from receiving the photons which are essential for photocatalytic activity to occur (Zhao et al., 2012; Maruthamani et al., 2015).

Based on the boundaries and independent variables set for the optimization study, the optimum conditions for maximum photocatalytic degradation of RhB were identified as pH 3.7, initial dye concentration of 10 mg/L and photocatalyst dosage of 0.20 g (Fig. 12(c) and Fig. S2). A further experimental investigation was conducted based on the generated ideal conditions and a relatively high conformity between the experimental data and model predicted value was observed.

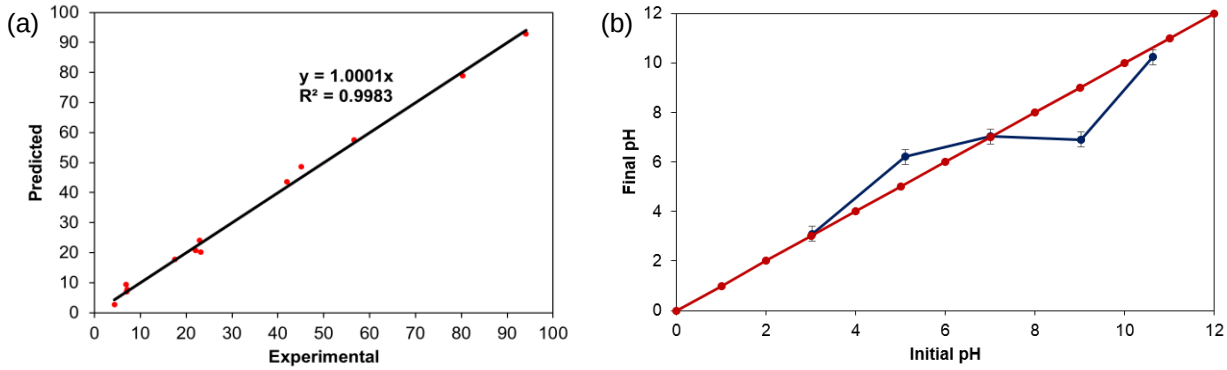

(c)

pH value	Initial dye concentration (mg/L)	Dosage of photocatalyst (g)	RhB photodegradation (%)	
			Experimental	Predicted
3.37	10	0.20	96.22	100

Fig. 12 (a) Graph of predicted against experimental data for each run, (b) Plot for determination of pH_{pzc} of 1-

BCQD/CN and (c) Optimum conditions for maximum RhB photodegradation and comparison between the experimental and predict data.

4.0 Conclusion

In summary, novel metal-free composite photocatalysts (BCQD/CN) were successfully fabricated by hybridizing B-doped CQDs and n/n-type g-C_3N_4 homojunction derived from equal proportion of urea and thiourea. Different amounts of B dopant were applied to determine the appropriate dosage in optimizing the photocatalytic efficiency of BCQD/CN nanocomposite. The successful incorporation of BCQDs and CQDs into g-C_3N_4/g-C_3N_4 homojunction was verified via a series of characterization analyses including FESEM, TEM, EDX, XRD, FTIR and XPS. These tests have successfully proven the co-existence of BCQDs and CN which were bonded together securely as distinguished through the changes in their surface morphologies, crystalline structures, chemical compositions, etc. PL and UV-Vis DRS were also carried out to study the optical properties of the as-synthesized photocatalyst samples by evaluating their band gap structures and charge transfer behaviours. The optimized photocatalytic nanocomposite, 1-BCQD/CN with a mass ratio of boric acid to citric acid at 1:3 displayed a marginally higher photocatalytic performance relative to other BCQD/CN samples with a RhB photodegradation efficiency 31 % and 40 % higher than that of CQD/CN and CN respectively. There are several contributing factors to the boosted photoactivity of BCQD/CN nanocomposites, including the synergistic effects of (1) promoted electron charge transport from CN to BCQDs, (2) suppressed recombination rate of electron-hole pairs and (3) improved charge density in facilitating charge migration. The photoactivity evaluation of RhB degradation was conducted under the illumination of an 18W LED light. The remarkable photo-efficiency displayed by BCQD/CN toward RhB degradation despite the relatively low-powered with a relatively low-powered light source highlights the various benefits from the environmental

and economic perspectives. This offers an optimistic outlook to the possible industrial-scale operation for wastewater treatment by means of photocatalysis in the near future. On top of that, the durability of 1-BCQD/CN was also validated by subjecting it to 3 consecutive cycles of RhB photodegradation under identical conditions, where no observable regression in photoactivity was observed. A plausible photocatalytic mechanism for RhB degradation in the presence of BCQD/CN was also proposed by identifying the roles of specific reactive species through a series of scavenging tests. An optimization study was performed for the process of RhB photodegradation and a quadratic regression model was developed to identify the optimum conditions for maximum removal of RhB as pH 3.37, initial RhB concentration of 10 mg/L and 0.20 g of 1-BCQD/CN photocatalyst. On the whole, this research work is expected to provoke more pioneering research ideas in the development of photocatalytic semiconductors as a robust approach to various pressing global challenges, particularly the environmental- and energy-related matters.

Declarations

Ethics approval and consent to participate

Not applicable

Consent for publication

Not applicable

Availability of data and materials

All data generated or analyzed during this study are included in this published article [and its supplementary information files].

Competing interests

The authors declare that they have no competing interests.

Funding

This work was funded by the Ministry of Higher Education (MOHE) Malaysia under the Fundamental-Research Grant Scheme (FRGS) (Ref no: FRGS/1/2018/TK02/HWUM/03/2).

Authors' contributions

All authors contributed to the study conception and design. Material preparation, data collection and analysis were performed by SP and JL. The research work was supervised by VW, LT and SC. The first draft of the manuscript was written by SP and all authors commented on previous versions of the manuscript. All authors read and approved the final manuscript.

References

An H-R, Park S Y, Kim H, Lee C Y, Choi S, Lee S C, Seo S, Park E C, Oh Y-K, Song C-G, Won J, Kim Y J, Lee J, Lee H U, Lee Y-C (2016). Advanced nanoporous TiO2 photocatalysts by hydrogen plasma for efficient solar-light photocatalytic application. Scientific Reports, 6(1): 29683

Armstrong D A, Huie R E, Koppenol W H, Lymar S V, Merényi G, Neta P, Ruscic B, Stanbury D M, Steenken S, Wardman P (2015). Standard electrode potentials involving radicals in aqueous solution: inorganic radicals (IUPAC Technical Report). Pure and Applied Chemistry, 87(11-12): 1139-1150

Babu P, Mohanty S, Naik B, Parida K (2018). Synergistic Effects of Boron and Sulfur Co-doping into Graphitic Carbon Nitride Framework for Enhanced Photocatalytic Activity in Visible Light Driven Hydrogen Generation. ACS Applied Energy Materials, 1(11): 5936-5947

Bhati A, Anand S R, Saini D, Sonkar S K (2019). Sunlight-induced photoreduction of Cr (VI) to Cr (III) in wastewater by nitrogen-phosphorus-doped carbon dots. npj Clean Water, 2(1): 1-9

Cao S, Shen B, Tong T, Fu J, Yu J (2018). 2D/2D heterojunction of ultrathin MXene/Bi2WO6 nanosheets for improved photocatalytic CO2 reduction. Advanced Functional Materials, 28(21): 1800136

Che H, Liu L, Che G, Dong H, Liu C, Li C (2019). Control of energy band, layer structure and vacancy defect of graphitic carbon nitride by intercalated hydrogen bond effect of NO3− toward improving photocatalytic performance. Chemical Engineering Journal, 357: 209-219

Chen P-W, Li K, Yu Y-X, Zhang W-D (2017). Cobalt-doped graphitic carbon nitride photocatalysts with high activity for hydrogen evolution. Applied Surface Science, 392: 608-615

Chiu Y-H, Chang T-F M, Chen C-Y, Sone M, Hsu Y-J (2019). Mechanistic insights into photodegradation of organic dyes using heterostructure photocatalysts. Catalysts, 9(5): 430

Choi Y, Kang B, Lee J, Kim S, Kim G T, Kang H, Lee B R, Kim H, Shim S-H, Lee G, Kwon O-H, Kim B-S (2016). Integrative Approach toward Uncovering the Origin of Photoluminescence in Dual Heteroatom-Doped Carbon Nanodots. Chemistry of Materials, 28(19): 6840-6847

Chong M N, Jin B, Chow C W K, Saint C (2010). Recent developments in photocatalytic water treatment technology: A review. Water Research, 44(10): 2997-3027

Cushing S K, Meng F, Zhang J, Ding B, Chen C K, Chen C-J, Liu R-S, Bristow A D, Bright J, Zheng P, Wu N (2017). Effects of Defects on Photocatalytic Activity of Hydrogen-Treated Titanium Oxide Nanobelts. ACS Catalysis, 7(3): 1742-1748

Da Silva W L, Hamilton J W J, Sharma P K, Dunlop P S M, Byrne J A, Dos Santos J H Z (2021). Agro and industrial residues: Potential raw materials for photocatalyst development. Journal of Photochemistry and Photobiology A: Chemistry, 411: 113184

Da Silva W L, Lansarin M A, Dos Santos J H Z, Silveira F (2016). Photocatalytic degradation of rhodamine B, paracetamol and diclofenac sodium by supported titania-based catalysts from petrochemical residue: effect of doping with magnesium. Water Science and Technology, 74(10): 2370-2383

Da Silva W L, Lansarin M A, Stedile F C, Dos Santos J H Z (2014). The potential of chemical industrial and academic wastes as a source of supported photocatalysts. Journal of Molecular Catalysis A: Chemical, 393: 125-133

Dahri M K, Kooh M R R, Lim L B L (2016). Remediation of Rhodamine B Dye from Aqueous Solution Using Casuarina equisetifolia Cone Powder as a Low-Cost Adsorbent. Advances in Physical Chemistry, 2016: 9497378

Das A, Gude V, Roy D, Chatterjee T, De C K, Mandal P K (2017). On the Molecular Origin of Photoluminescence of Nonblinking Carbon Dot. The Journal of Physical Chemistry C, 121(17): 9634-9641

Di G, Zhu Z, Dai Q, Zhang H, Shen X, Qiu Y, Huang Y, Yu J, Yin D, Küppers S (2020). Wavelength-dependent effects of carbon quantum dots on the photocatalytic activity of g-C3N4 enabled by LEDs. Chemical Engineering Journal, 379: 122296

Elshafie M, Younis S A, Serp P, Gad E a M (2020). Preparation characterization and non-isothermal decomposition kinetics of different carbon nitride sheets. Egyptian Journal of Petroleum, 29(1): 21-29

Fontelles-Carceller O, Muñoz-Batista M J, Fernández-García M, Kubacka A (2016). Interface Effects in Sunlight-Driven Ag/g-C3N4 Composite Catalysts: Study of the Toluene Photodegradation Quantum Efficiency. ACS Applied Materials & Interfaces, 8(4): 2617-2627

Fronczak M, Demby K, Strachowski P, Strawski M, Bystrzejewski M (2018). Graphitic Carbon Nitride Doped with the s-Block Metals: Adsorbent for the Removal of Methyl Blue and Copper(II) Ions. Langmuir, 34(25): 7272-7283

Gao L, Li Z, Liu J (2017). Facile synthesis of Ag3VO4/β-AgVO3 nanowires with efficient visible-light photocatalytic activity. RSC Advances, 7(44): 27515-27521

Ghosh U, Pal A (2020). Defect engineered mesoporous 2D graphitic carbon nitride nanosheet photocatalyst for rhodamine B degradation under LED light illumination. Journal of Photochemistry and Photobiology A: Chemistry, 397: 112582

Guan M, Wang C, Li S, Du H, Yuan Y (2020). Understanding the Enhanced Electrocatalytic Hydrogen Evolution via Integrating Electrochemically Inactive g-C3N4: The Effect of Interfacial Engineering. ACS Sustainable Chemistry & Engineering, 8(27): 10313-10320

Guo Y, Cao F, Li Y (2018). Solid phase synthesis of nitrogen and phosphor co-doped carbon quantum dots for sensing Fe3+ and the enhanced photocatalytic degradation of dyes. Sensors and Actuators B: Chemical, 255: 1105-1111

Hasija V, Raizada P, Sudhaik A, Sharma K, Kumar A, Singh P, Jonnalagadda S B, Thakur V K (2019). Recent advances in noble metal free doped graphitic carbon nitride based nanohybrids for photocatalysis of organic contaminants in water: A review. Applied Materials Today, 15: 494-524

Hu J, Chen D, Mo Z, Li N, Xu Q, Li H, He J, Xu H, Lu J (2019). Z-Scheme 2D/2D Heterojunction of Black Phosphorus/Monolayer Bi2WO6 Nanosheets with Enhanced Photocatalytic Activities. Angewandte Chemie International Edition, 58(7): 2073-2077

Huy B T, Thao C T B, Dao V-D, Phuong N T K, Lee Y-I (2017). A Mixed-Metal Oxides/Graphitic Carbon Nitride: High Visible Light Photocatalytic Activity for Efficient Mineralization of Rhodamine B. Advanced Materials Interfaces, 4(12): 1700128

Jeevitha G, Abhinayaa R, Mangalaraj D, Ponpandian N (2018). Tungsten oxide-graphene oxide (WO3-GO) nanocomposite as an efficient photocatalyst, antibacterial and anticancer agent. Journal of Physics and Chemistry of Solids, 116: 137-147

Jiao X, Zheng K, Hu Z, Sun Y, Xie Y (2020). Broad-Spectral-Response Photocatalysts for CO2 Reduction. ACS Central Science, 6(5): 653-660

Kesarla M K, Fuentez-Torres M O, Alcudia-Ramos M A, Ortiz-Chi F, Espinosa-González C G, Aleman M, Torres-Torres J G, Godavarthi S (2019). Synthesis of g-C3N4/N-doped CeO2 composite for photocatalytic degradation of an herbicide. Journal of Materials Research and Technology, 8(2): 1628-1635

Klubnuan S, Suwanboon S, Amornpitoksuk P (2016). Effects of optical band gap energy, band tail energy and particle shape on photocatalytic activities of different ZnO nanostructures prepared by a hydrothermal method. Optical Materials, 53: 134-141

Kooh M R R, Lim L B L, Lim L H, Dahri M K (2016). Separation of toxic rhodamine B from aqueous solution using an efficient low-cost material, Azolla pinnata, by adsorption method. Environmental Monitoring and Assessment, 188(2): 108

Kooshki H, Sobhani-Nasab A, Eghbali-Arani M, Ahmadi F, Ameri V, Rahimi-Nasrabadi M (2019). Eco-friendly synthesis of PbTiO3 nanoparticles and PbTiO3/carbon quantum dots binary nano-hybrids for enhanced photocatalytic performance under visible light. Separation and Purification Technology, 211: 873-881

Krumova K, Cosa G (2016). Singlet Oxygen: Applications in Biosciences and Nanosciences, Volume 1: The Royal Society of Chemistry, 1-21

Kumar S, Kumar A, Bahuguna A, Sharma V, Krishnan V (2017). Two-dimensional carbon-based nanocomposites for photocatalytic energy generation and environmental remediation applications. Beilstein journal of nanotechnology, 8(1): 1571-1600

Kumru B, Barrio J, Zhang J, Antonietti M, Shalom M, Schmidt B V K J (2019). Robust Carbon Nitride-Based Thermoset Coatings for Surface Modification and Photochemistry. ACS Applied Materials & Interfaces, 11(9): 9462-9469

Kundu S, Xia W, Busser W, Becker M, Schmidt D A, Havenith M, Muhler M (2010). The formation of nitrogen-containing functional groups on carbon nanotube surfaces: a quantitative XPS and TPD study. Physical Chemistry Chemical Physics, 12(17): 4351-4359

Li W, Ma Q, Wang X, Chu X-S, Wang F, Wang X-C, Wang C-Y (2020a). Enhanced photoresponse and fast charge transfer: three-dimensional macroporous g-C3N4/GO-TiO2 nanostructure for hydrogen evolution. Journal of Materials Chemistry A, 8(37): 19533-19543

Li X, Ouyang S, Kikugawa N, Ye J (2008). Novel Ag2ZnGeO4 photocatalyst for dye degradation under visible light irradiation. Applied Catalysis A: General, 334(1): 51-58

Li X, Zhao Z (2014). Facile ionic-liquid-assisted electrochemical synthesis of size-controlled carbon quantum dots by tuning applied voltages. RSC Advances, 4(101): 57615-57619

Li Y, Liu J, Wan X, Pan R, Bai B, Wang H, Cao X, Zhang J (2020b). Surface passivation enabled-structural engineering of I-III-VI2 nanocrystal photocatalysts. Journal of Materials Chemistry A, 8(19): 9951-9962

Lim S Y, Shen W, Gao Z (2015). Carbon quantum dots and their applications. Chemical Society Reviews, 44(1): 362-381

Lin X, Liu C, Wang J, Yang S, Shi J, Hong Y (2019). Graphitic carbon nitride quantum dots and nitrogen-doped carbon quantum dots co-decorated with BiVO4 microspheres: a ternary heterostructure photocatalyst for water purification. Separation and Purification Technology, 226: 117-127

Liu B, Qiao M, Wang Y, Wang L, Gong Y, Guo T, Zhao X (2017). Persulfate enhanced photocatalytic degradation of bisphenol A by g-C3N4 nanosheets under visible light irradiation. Chemosphere, 189: 115-122

Liu J, Zhang T, Wang Z, Dawson G, Chen W (2011). Simple pyrolysis of urea into graphitic carbon nitride with recyclable adsorption and photocatalytic activity. Journal of Materials Chemistry, 21(38): 14398-14401

Liu Q, Tian H, Dai Z, Sun H, Liu J, Ao Z, Wang S, Han C, Liu S (2020). Nitrogen-doped Carbon Nanospheres-Modified Graphitic Carbon Nitride with Outstanding Photocatalytic Activity. Nano-Micro Letters, 12(1): 24

Liu Y, Yu Y-X, Zhang W-D (2014). Photoelectrochemical study on charge transfer properties of nanostructured Fe2O3 modified by g-C3N4. International Journal of Hydrogen Energy, 39(17): 9105-9113

Liu Z, Sun D D, Guo P, Leckie J O (2007). One-Step Fabrication and High Photocatalytic Activity of Porous TiO2 Hollow Aggregates by Using a Low-Temperature Hydrothermal Method Without Templates. Chemistry – A European Journal, 13(6): 1851-1855

Liu Z, Wang G, Chen H-S, Yang P (2018). An amorphous/crystalline g-C3N4 homojunction for visible light photocatalysis reactions with superior activity. Chemical Communications, 54(37): 4720-4723

Luo P G, Sahu S, Yang S-T, Sonkar S K, Wang J, Wang H, Lecroy G E, Cao L, Sun Y-P (2013). Carbon "quantum" dots for optical bioimaging. Journal of Materials Chemistry B, 1(16): 2116-2127

Ma J, Li L, Zou J, Kong Y, Komarneni S (2014). Highly efficient visible light degradation of Rhodamine B by nanophasic Ag3PO4 dispersed on SBA-15. Microporous and mesoporous materials, 193: 154-159

Ma X, Lou Y, Chen J (2018). New UiO-66/CuxS Heterostructures: Surface Functionalization Synthesis and Their Application in Photocatalytic Degradation of RhB. Bulletin of the Chemical Society of Japan, 91(4): 515-522
Ma Y, Li X, Yang Z, Xu S, Zhang W, Su Y, Hu N, Lu W, Feng J, Zhang Y (2016). Morphology control and photocatalysis enhancement by in situ hybridization of cuprous oxide with nitrogen-doped carbon quantum dots. Langmuir, 32(37): 9418-9427
Ma Z, Ming H, Huang H, Liu Y, Kang Z (2012). One-step ultrasonic synthesis of fluorescent N-doped carbon dots from glucose and their visible-light sensitive photocatalytic ability. New Journal of Chemistry, 36(4): 861-864
Madjene F, Assassi M, Chokri I, Enteghar T, Lebik H (2021). Optimization of photocatalytic degradation of rhodamine B using Box–Behnken experimental design: Mineralization and mechanism. Water Environment Research, 93(1): 112-122
Martins N C T, Ângelo J, Girão A V, Trindade T, Andrade L, Mendes A (2016). N-doped carbon quantum dots/TiO2 composite with improved photocatalytic activity. Applied Catalysis B: Environmental, 193: 67-74
Maruthamani D, Divakar D, Kumaravel M (2015). Enhanced photocatalytic activity of TiO2 by reduced graphene oxide in mineralization of Rhodamine B dye. Journal of Industrial and Engineering Chemistry, 30: 33-43
Mishra A, Mehta A, Basu S, Shetti N P, Reddy K R, Aminabhavi T M (2019). Graphitic carbon nitride (g–C3N4)–based metal-free photocatalysts for water splitting: a review. Carbon, 149: 693-721
Molaei M J (2020). The optical properties and solar energy conversion applications of carbon quantum dots: A review. Solar Energy, 196: 549-566
Moreno Y P, Da Silva W L, Stedile F C, Radtke C, Dos Santos J H Z (2021). Micro and nanodomains on structured silica/titania photocatalysts surface evaluated in RhB degradation: Effect of structural properties on catalytic efficiency. Applied Surface Science Advances, 3: 100055
Muraro P C L, Mortari S R, Vizzotto B S, Chuy G, Dos Santos C, Brum L F W, Da Silva W L (2020). Iron oxide nanocatalyst with titanium and silver nanoparticles: Synthesis, characterization and photocatalytic activity on the degradation of Rhodamine B dye. Scientific Reports, 10(1): 3055
Nassar M Y, Abdelrahman E A (2017). Hydrothermal tuning of the morphology and crystallite size of zeolite nanostructures for simultaneous adsorption and photocatalytic degradation of methylene blue dye. Journal of Molecular Liquids, 242: 364-374
Ong W-J, Putri L K, Tan Y-C, Tan L-L, Li N, Ng Y H, Wen X, Chai S-P (2017). Unravelling charge carrier dynamics in protonated g-C3N4 interfaced with carbon nanodots as co-catalysts toward enhanced photocatalytic CO2 reduction: A combined experimental and first-principles DFT study. Nano Research, 10(5): 1673-1696
Organization W H (2019). Drinking Water: World Health Organization
Orooji Y, Ghanbari M, Amiri O, Salavati-Niasari M (2020). Facile fabrication of silver iodide/graphitic carbon nitride nanocomposites by notable photo-catalytic performance through sunlight and antimicrobial activity. Journal of Hazardous Materials, 389: 122079
Pan J, Zheng Z, Yang J, Wu Y, Lu F, Chen Y, Gao W (2017). A novel and sensitive fluorescence sensor for glutathione detection by controlling the surface passivation degree of carbon quantum dots. Talanta, 166: 1-7

928 Peng Z, Zhou Y, Ji C, Pardo J, Mintz K J, Pandey R R, Chusuei C C, Graham R M, Yan G, Leblanc R M
929 (2020). Facile synthesis of “boron-doped” carbon dots and their application in visible-light-driven
930 photocatalytic degradation of organic dyes. Nanomaterials, 10(8): 1560
931 Phang S J, Goh J M, Tan L-L, Lee W P C, Ong W-J, Chai S-P (2020a). Metal-free n/n–junctioned
932 graphitic carbon nitride (g-C3N4): a study to elucidate its charge transfer mechanism and
933 application for environmental remediation. Environmental Science and Pollution Research,
934 Phang S J, Tan L-L (2019). Recent advances in carbon quantum dots (CQDs)-based two
935 dimensional materials for photocatalytic applications. Catalysis Science & Technology,
936 Phang S J, Wong V-L, Tan L-L, Chai S-P (2020b). Recent advances in homojunction-based
937 photocatalysis for sustainable environmental remediation and clean energy generation. Applied
938 Materials Today, 20: 100741
939 Qiao F, Wang J, Ai S, Li L (2015). As a new peroxidase mimetics: The synthesis of selenium doped
940 graphitic carbon nitride nanosheets and applications on colorimetric detection of H2O2 and
941 xanthine. Sensors and Actuators B: Chemical, 216: 418-427
942 Qin J, Zeng H (2017). Photocatalysts fabricated by depositing plasmonic Ag nanoparticles on
943 carbon quantum dots/graphitic carbon nitride for broad spectrum photocatalytic hydrogen
944 generation. Applied Catalysis B: Environmental, 209: 161-173
945 Ramanathan S, Selvin S P, Obadiah A, Durairaj A, Santhoshkumar P, Lydia S, Ramasundaram S,
946 Vasanthkumar S (2019). Synthesis of reduced graphene oxide/ZnO nanocomposites using grape
947 fruit extract and Eichhornia crassipes leaf extract and a comparative study of their photocatalytic
948 property in degrading Rhodamine B dye. Journal of Environmental Health Science and
949 Engineering, 17(1): 195-207
950 Ran J, Ma T Y, Gao G, Du X-W, Qiao S Z (2015). Porous P-doped graphitic carbon nitride
951 nanosheets for synergistically enhanced visible-light photocatalytic H2 production. Energy &
952 Environmental Science, 8(12): 3708-3717
953 Ran J, Pan T, Wu Y, Chu C, Cui P, Zhang P, Ai X, Fu C-F, Yang Z, Xu T (2019). Endowing g-C3N4
954 Membranes with Superior Permeability and Stability by Using Acid Spacers. Angewandte Chemie
955 International Edition, 58(46): 16463-16468
956 Rangaraju R R, Panday A, Raja K S, Misra M (2009). Nanostructured anodic iron oxide film as
957 photoanode for water oxidation. Journal of Physics D: Applied Physics, 42(13): 135303
958 Saher R, Hanif M A, Mansha A, Javed H M A, Zahid M, Nadeem N, Mustafa G, Shaheen A, Riaz O
959 (2021). Sunlight-driven photocatalytic degradation of rhodamine B dye by Ag/FeWO4/g-C3N4
960 composites. International Journal of Environmental Science and Technology, 18(4): 927-938
961 Sahu R S, Shih Y-H, Chen W-L (2020). New insights of metal free 2D graphitic carbon nitride for
962 photocatalytic degradation of bisphenol A. Journal of Hazardous Materials: 123509
963 Seng R X, Tan L-L, Lee W P C, Ong W-J, Chai S-P (2020). Nitrogen-doped carbon quantum dots-
964 decorated 2D graphitic carbon nitride as a promising photocatalyst for environmental
965 remediation: A study on the importance of hybridization approach. Journal of Environmental
966 Management, 255: 109936
967 Song B, Wang Q, Wang L, Lin J, Wei X, Murugadoss V, Wu S, Guo Z, Ding T, Wei S (2020). Carbon
968 nitride nanoplatelet photocatalysts heterostructured with B-doped carbon nanodots for
969 enhanced photodegradation of organic Pollutants. Journal of Colloid and Interface Science, 559:
970 124-133

971 Sun Q, Lv K, Zhang Z, Li M, Li B (2015). Effect of contact interface between TiO2 and g-C3N4 on
972 the photoreactivity of g-C3N4/TiO2 photocatalyst:(0 0 1) vs (1 0 1) facets of TiO2. Applied
973 Catalysis B: Environmental, 164: 420-427
974 Tan L, Xu J, Zhang X, Hang Z, Jia Y, Wang S (2015). Synthesis of g-C3N4/CeO2 nanocomposites
975 with improved catalytic activity on the thermal decomposition of ammonium perchlorate.
976 Applied Surface Science, 356: 447-453
977 Tan S, Xing Z, Zhang J, Li Z, Wu X, Cui J, Kuang J, Yin J, Zhou W (2017). Meso-g-C3N4/g-C3N4
978 nanosheets laminated homojunctions as efficient visible-light-driven photocatalysts.
979 International Journal of Hydrogen Energy, 42(41): 25969-25979
980 Tho N T M, Huy B T, Khanh D N N, Ha H N N, Huy V Q, Vy N T T, Huy D M, Dat D P, Phuong N T K
981 (2018). Facile synthesis of ZnBi2O4-graphite composites as highly active visible-light
982 photocatalyst for the mineralization of rhodamine B. Korean Journal of Chemical Engineering,
983 35(12): 2442-2451
984 Tian N, Huang H, Liu C, Dong F, Zhang T, Du X, Yu S, Zhang Y (2015). In situ co-pyrolysis fabrication
985 of CeO 2/gC 3 N 4 n–n type heterojunction for synchronously promoting photo-induced oxidation
986 and reduction properties. Journal of Materials Chemistry A, 3(33): 17120-17129
987 Tian N, Zhang Y, Li X, Xiao K, Du X, Dong F, Waterhouse G I N, Zhang T, Huang H (2017). Precursor-
988 reforming protocol to 3D mesoporous g-C3N4 established by ultrathin self-doped nanosheets for
989 superior hydrogen evolution. Nano Energy, 38: 72-81
990 Tyborski T, Merschjann C, Orthmann S, Yang F, Lux-Steiner M C, Schedel-Niedrig T (2013). Crystal
991 structure of polymeric carbon nitride and the determination of its process-temperature-induced
992 modifications. Journal of Physics: Condensed Matter, 25(39): 395402
993 Vaez M, Zarringhalam Moghaddam A, Alijani S (2012). Optimization and Modeling of
994 Photocatalytic Degradation of Azo Dye Using a Response Surface Methodology (RSM) Based on
995 the Central Composite Design with Immobilized Titania Nanoparticles. Industrial & Engineering
996 Chemistry Research, 51(11): 4199-4207
997 Viezbicke B D, Patel S, Davis B E, Birnie Iii D P (2015). Evaluation of the Tauc method for optical
998 absorption edge determination: ZnO thin films as a model system. physica status solidi (b), 252(8):
999 1700-1710
1000 Wang F, Chen P, Feng Y, Xie Z, Liu Y, Su Y, Zhang Q, Wang Y, Yao K, Lv W, Liu G (2017a). Facile
1001 synthesis of N-doped carbon dots/g-C3N4 photocatalyst with enhanced visible-light
1002 photocatalytic activity for the degradation of indomethacin. Applied Catalysis B: Environmental,
1003 207: 103-113
1004 Wang F, Wang Y, Feng Y, Zeng Y, Xie Z, Zhang Q, Su Y, Chen P, Liu Y, Yao K, Lv W, Liu G (2018).
1005 Novel ternary photocatalyst of single atom-dispersed silver and carbon quantum dots co-loaded
1006 with ultrathin g-C3N4 for broad spectrum photocatalytic degradation of naproxen. Applied
1007 Catalysis B: Environmental, 221: 510-520
1008 Wang G, Zhang W, Li J, Dong X, Zhang X (2019a). Carbon quantum dots decorated BiVO4 quantum
1009 tube with enhanced photocatalytic performance for efficient degradation of organic pollutants
1010 under visible and near-infrared light. Journal of Materials Science, 54(8): 6488-6499
1011 Wang S, Kudrawiec R, Chi C, Zhang L, Zhang X, Ou X (2020). Mid-infrared Optoelectronics. Tournié,
1012 E. and Cerutti, L. (eds): Woodhead Publishing, 457-492
1013 Wang W, Zeng Z, Zeng G, Zhang C, Xiao R, Zhou C, Xiong W, Yang Y, Lei L, Liu Y (2019b). Sulfur
1014 doped carbon quantum dots loaded hollow tubular g-C3N4 as novel photocatalyst for destruction

of Escherichia coli and tetracycline degradation under visible light. Chemical Engineering Journal, 378: 122132
Wang X, Cheng J, Yu H, Yu J (2017b). A facile hydrothermal synthesis of carbon dots modified g-C3N4 for enhanced photocatalytic H2-evolution performance. Dalton Transactions, 46(19): 6417-6424
Wang X, Wang F, Sang Y, Liu H (2017c). Full-Spectrum Solar-Light-Activated Photocatalysts for Light–Chemical Energy Conversion. Advanced Energy Materials, 7(23): 1700473
Wang Y, Kalytchuk S, Zhang Y, Shi H, Kershaw S V, Rogach A L (2014). Thickness-Dependent Full-Color Emission Tunability in a Flexible Carbon Dot Ionogel. The Journal of Physical Chemistry Letters, 5(8): 1412-1420
Weon S, He F, Choi W (2019). Status and challenges in photocatalytic nanotechnology for cleaning air polluted with volatile organic compounds: visible light utilization and catalyst deactivation. Environmental Science: Nano, 6(11): 3185-3214
Wu D, Wang B, Wang W, An T, Li G, Ng T W, Yip H Y, Xiong C, Lee H K, Wong P K (2015). Visible-light-driven BiOBr nanosheets for highly facet-dependent photocatalytic inactivation of Escherichia coli. Journal of Materials Chemistry A, 3(29): 15148-15155
Xiang Q, Yu J, Jaroniec M (2011). Preparation and Enhanced Visible-Light Photocatalytic H2-Production Activity of Graphene/C3N4 Composites. The Journal of Physical Chemistry C, 115(15): 7355-7363
Xu B, Wang X, Zhu C, Ran X, Li T, Guo L (2017). Probing the inhomogeneity and intermediates in the photosensitized degradation of rhodamine B by Ag3PO4 nanoparticles from an ensemble to a single molecule approach. RSC Advances, 7(65): 40896-40904
Xu Y, Gao S-P (2012). Band gap of C3N4 in the GW approximation. International Journal of Hydrogen Energy, 37(15): 11072-11080
Yan B, Du C, Yang G (2020). Constructing Built-in Electric Field in Ultrathin Graphitic Carbon Nitride Nanosheets by N and O Codoping for Enhanced Photocatalytic Hydrogen Evolution Activity. Small, 16(4): 1905700
Yang F, Lecroy G E, Wang P, Liang W, Chen J, Fernando K a S, Bunker C E, Qian H, Sun Y-P (2016). Functionalization of Carbon Nanoparticles and Defunctionalization—Toward Structural and Mechanistic Elucidation of Carbon “Quantum” Dots. The Journal of Physical Chemistry C, 120(44): 25604-25611
Yang J, Liang Y, Li K, Yang G, Wang K, Xu R, Xie X (2020a). One-step synthesis of novel K+ and cyano groups decorated triazine-/heptazine-based g-C3N4 tubular homojunctions for boosting photocatalytic H2 evolution. Applied Catalysis B: Environmental, 262: 118252
Yang Y, Li X, Zhou C, Xiong W, Zeng G, Huang D, Zhang C, Wang W, Song B, Tang X, Li X, Guo H (2020b). Recent advances in application of graphitic carbon nitride-based catalysts for degrading organic contaminants in water through advanced oxidation processes beyond photocatalysis: A critical review. Water Research, 184: 116200
Ye B, Han X, Yan M, Zhang H, Xi F, Dong X, Liu J (2017). Fabrication of metal-free two dimensional/two dimensional homojunction photocatalyst using various carbon nitride nanosheets as building blocks. Journal of Colloid and Interface Science, 507: 209-216
Zhang G, Lan Z-A, Wang X (2016a). Conjugated Polymers: Catalysts for Photocatalytic Hydrogen Evolution. Angewandte Chemie International Edition, 55(51): 15712-15727

Zhang H, Ming H, Lian S, Huang H, Li H, Zhang L, Liu Y, Kang Z, Lee S-T (2011). Fe2O3/carbon quantum dots complex photocatalysts and their enhanced photocatalytic activity under visible light. Dalton Transactions, 40(41): 10822-10825

Zhang H, Zhao L, Geng F, Guo L-H, Wan B, Yang Y (2016b). Carbon dots decorated graphitic carbon nitride as an efficient metal-free photocatalyst for phenol degradation. Applied Catalysis B: Environmental, 180: 656-662

Zhang J, Yu C, Lang J, Zhou Y, Zhou B, Hu Y H, Long M (2020a). Modulation of Lewis acidic-basic sites for efficient photocatalytic H2O2 production over potassium intercalated tri-s-triazine materials. Applied Catalysis B: Environmental, 277: 119225

Zhang L, Jin Z, Lu H, Lin T, Ruan S, Zhao X S, Zeng Y-J (2018). Improving the Visible-Light Photocatalytic Activity of Graphitic Carbon Nitride by Carbon Black Doping. ACS Omega, 3(11): 15009-15017

Zhang P, Song T, Wang T, Zeng H (2017a). In-situ synthesis of Cu nanoparticles hybridized with carbon quantum dots as a broad spectrum photocatalyst for improvement of photocatalytic H2 evolution. Applied Catalysis B: Environmental, 206: 328-335

Zhang X-S, Hu J-Y, Jiang H (2014). Facile modification of a graphitic carbon nitride catalyst to improve its photoreactivity under visible light irradiation. Chemical Engineering Journal, 256: 230-237

Zhang X, Ren Y, Ji Z, Fan J (2020b). Sensitive detection of amoxicillin in aqueous solution with novel fluorescent probes containing boron-doped carbon quantum dots. Journal of Molecular Liquids: 113278

Zhang Z, Yi G, Li P, Zhang X, Fan H, Zhang Y, Wang X, Zhang C (2020c). A minireview on doped carbon dots for photocatalytic and electrocatalytic applications. Nanoscale, 12(26): 13899-13906

Zhang Z, Zheng T, Xu J, Zeng H, Zhang N (2017b). Carbon quantum dots/Bi2MoO6 composites with photocatalytic H2 evolution and near infrared activity. Journal of Photochemistry and Photobiology A: Chemistry, 346: 24-31

Zhao D, Sheng G, Chen C, Wang X (2012). Enhanced photocatalytic degradation of methylene blue under visible irradiation on graphene@TiO2 dyade structure. Applied Catalysis B: Environmental, 111-112: 303-308

Zhen W, Sun J, Ning X, Shi X, Xue C (2021). Polymeric carbon nitride with internal n-p homojunctions for efficient photocatalytic CO2 reduction coupled with cyclohexene oxidation. Applied Catalysis B: Environmental, 298: 120568

Zhu D, Zhou Q (2020). Novel Bi2WO6 modified by N-doped graphitic carbon nitride photocatalyst for efficient photocatalytic degradation of phenol under visible light. Applied Catalysis B: Environmental, 268: 118426

Zhu P, Tan K, Chen Q, Xiong J, Gao L (2019). Origins of Efficient Multiemission Luminescence in Carbon Dots. Chemistry of Materials, 31(13): 4732-4742

Figure

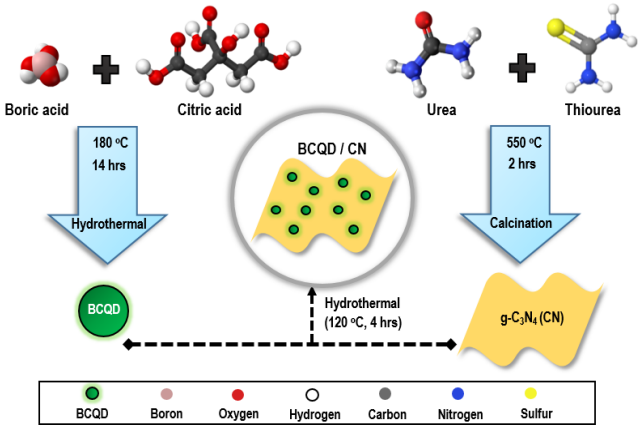

Fig. 1 Schematic illustration of synthesis route for BCQD/CN nanocomposites

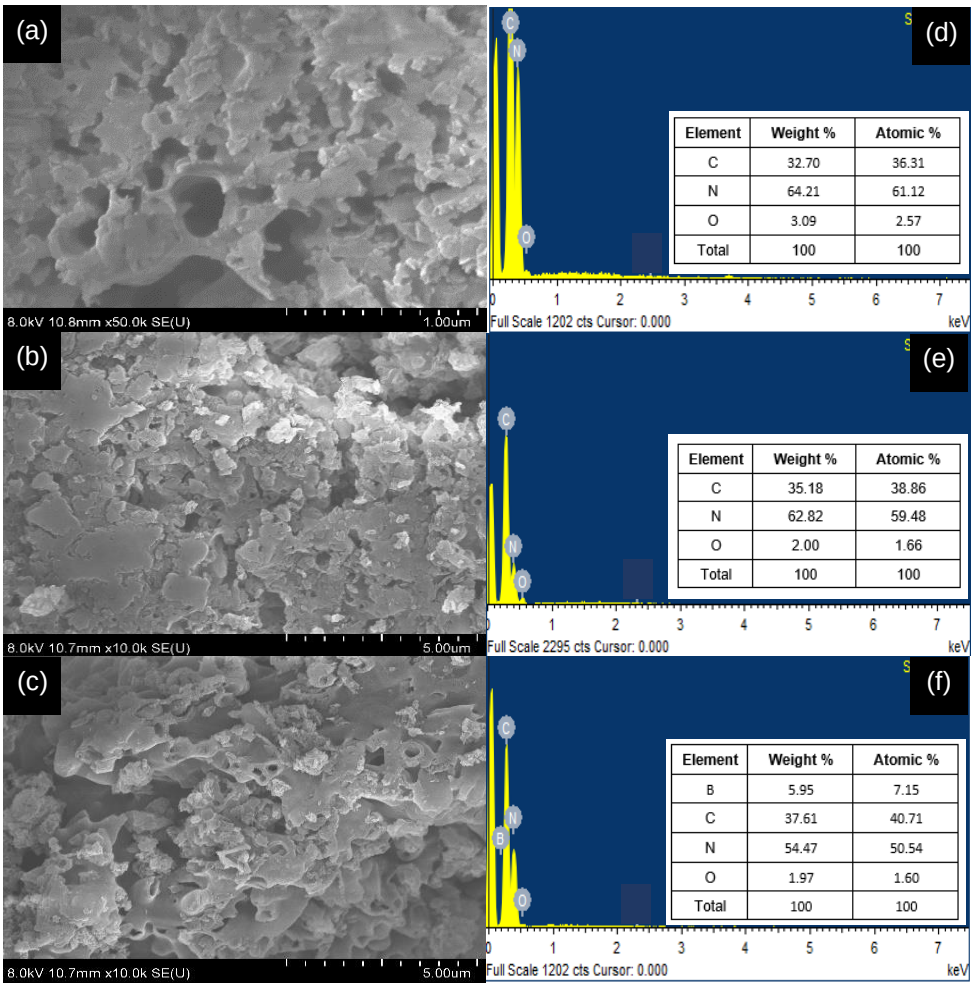

Fig. 2 FESEM images of (a) CN, (b) CQD/CN and (c) 1-BCQD/CN, EDX spectra for elemental analysis of (d) CN, (e) CQD/CN and (f) 1-BCQD/CN

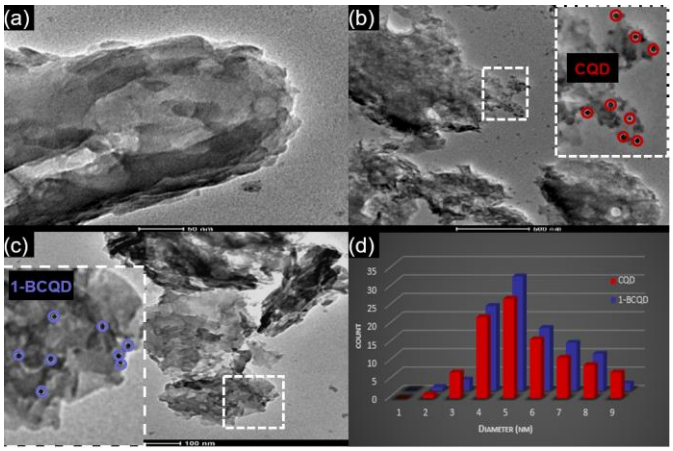

Fig. 3 TEM image of (a) CN, (b) CQD/CN, (c) 1-BCQD/CN and (d) Particle size distribution of BCQD and CQD on 1-BCQD/CN and CQD/CN, respectively

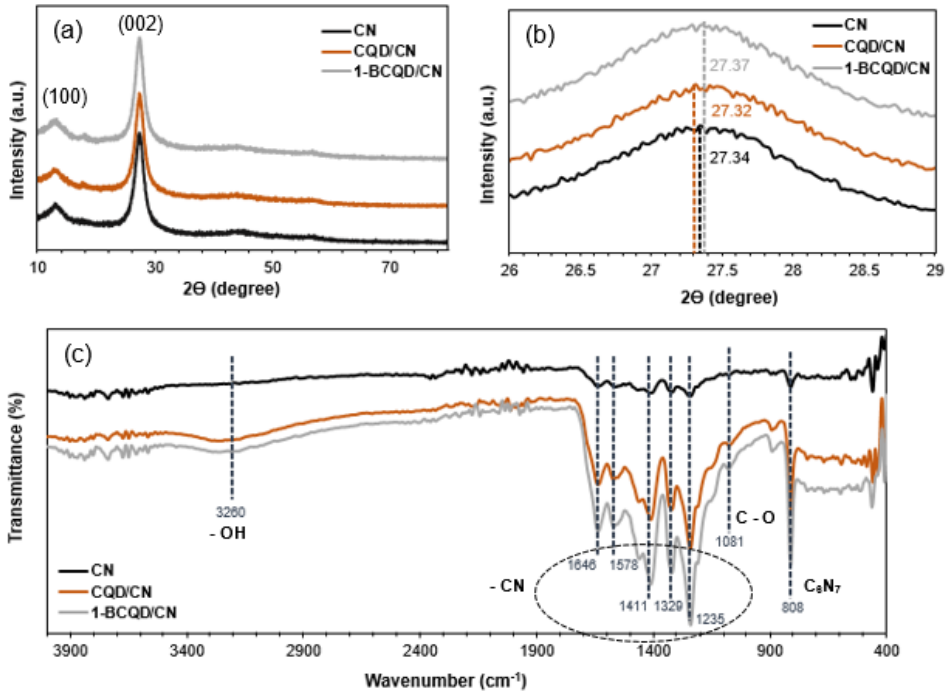

Fig. 4 (a) XRD spectra, (b) Magnified (002) peak of the XRD profile and (c) FTIR spectra of CN, CQD/CN and 1-BCQD/CN.

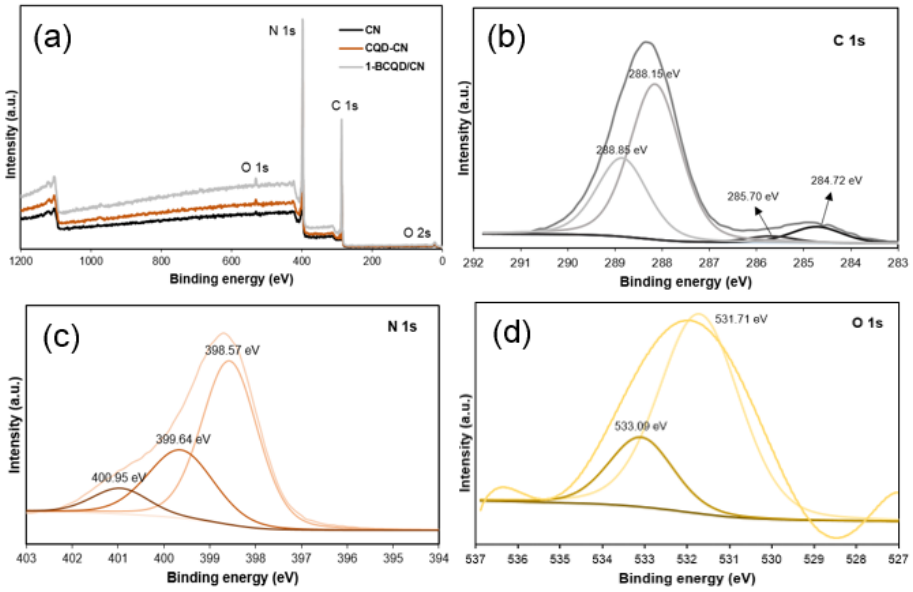

(e)

Photocatalyst sample	Atomic percentage (At %)			Weight percentage (Wt %)		
	C 1s	N 1s	O 1s	C 1s	N 1s	O 1s
CN	38.67	59.90	1.43	35.02	63.26	1.72
CQD/CN	40.19	59.11	0.70	36.52	62.63	0.85
1-BCQD/CN	40.44	58.04	1.52	36.71	61.44	1.85

Fig. 5 (a) XPS Survey spectra of CN, CQD/CN and 1-BCQD/CN; (b) C 1s spectra, (c) N 1s spectra and (d) O 1s spectra of 1-BCQD/CN; (e) Tabulated data of each element for CN, CQD/CN and 1-BCQD/CN

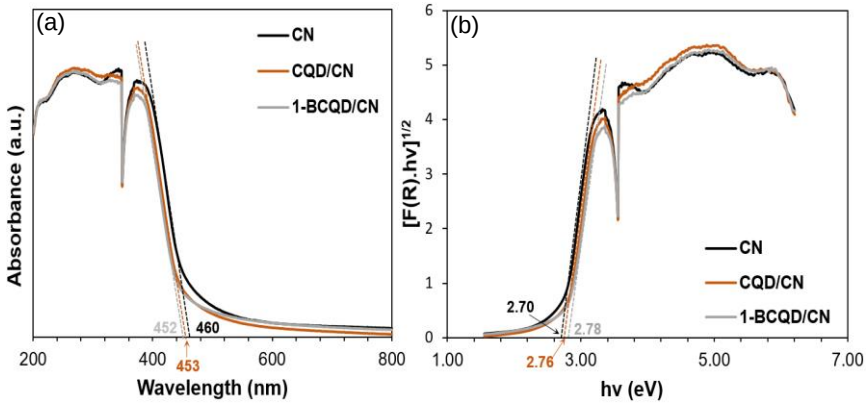

Fig. 6 (a) UV-Vis diffuse reflectance spectra and (b) Corresponding Tauc plot of CN, CQD/CN and 1-BCQD/CN

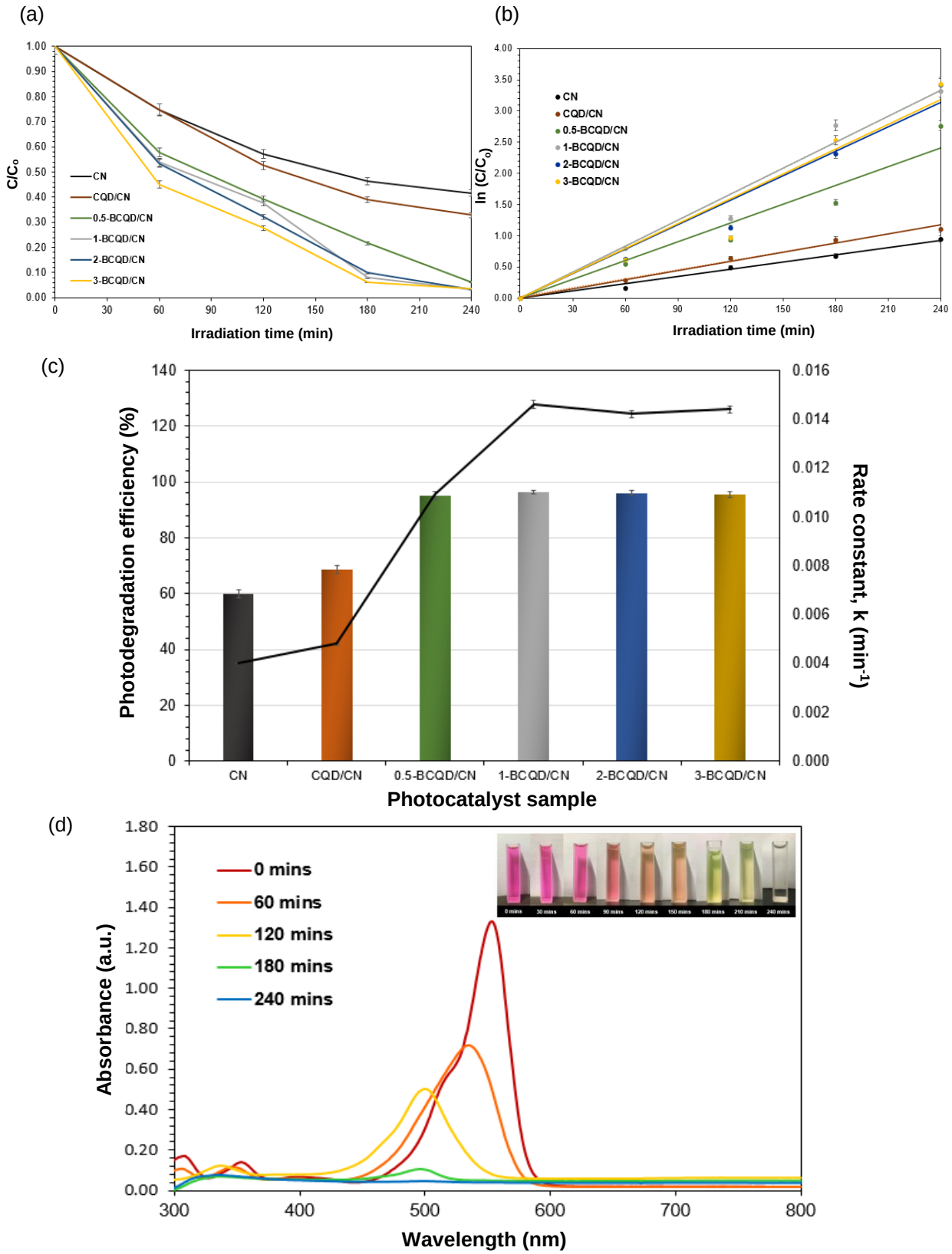

Fig. 7 (a) RhB degradation profile with respect to time, b) Linear graph of ln (C_o/C) against irradiation time for all

photocatalyst samples, (c) RhB degradation efficiency and kinetic rate constant of each photocatalyst under the irradiation of LED light and (d) Absorbance curves of 1-BCQD/CN at wavelengths between 300 and 800 nm for 240 mins with 60 min intervals (Inset: gradual decolorization of the RhB dye as a result of photodegradation in the presence of 1-BCQD/CN)

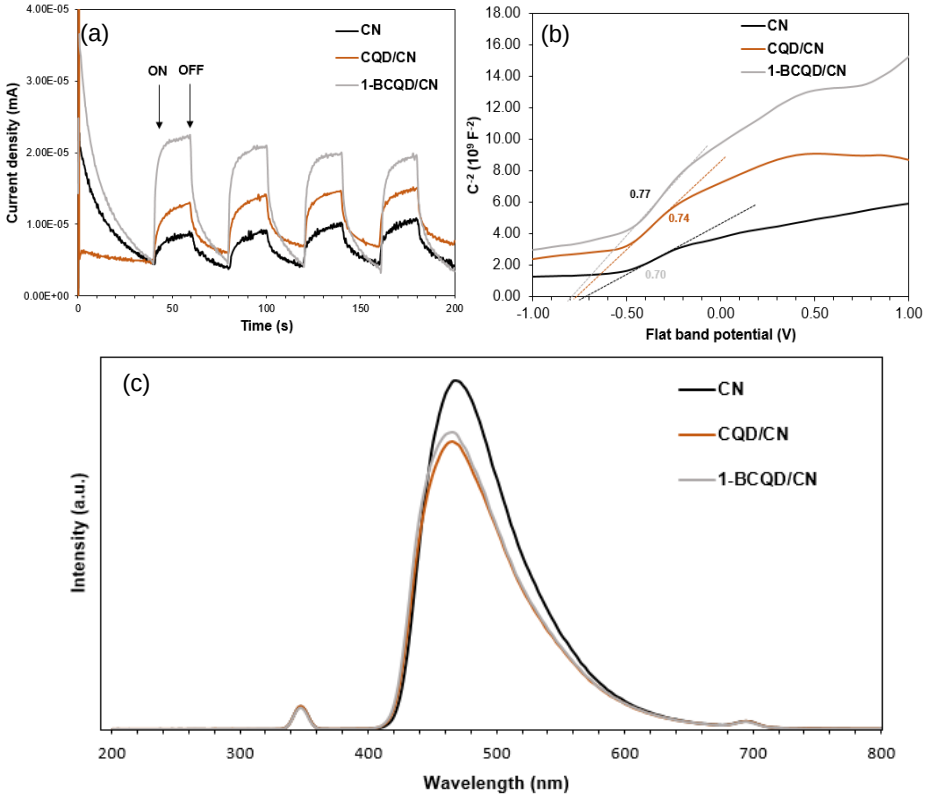

Fig. 8 (a) Transient photocurrent response, (b) Mott-Schottky plots and (c) PL spectra of CN, CQD/CN and 1-BCQD/CN

(a)

Scavenger	Reactive species	C/C_o at t = 240 mins	Degradation efficiency (%)
TEOA	h^+	0.808	19.16
BZQ	$\cdot O_2^-$	0.773	22.74
IPA	·OH	0.178	82.17
Without	N/A	0.032	96.77

(b)

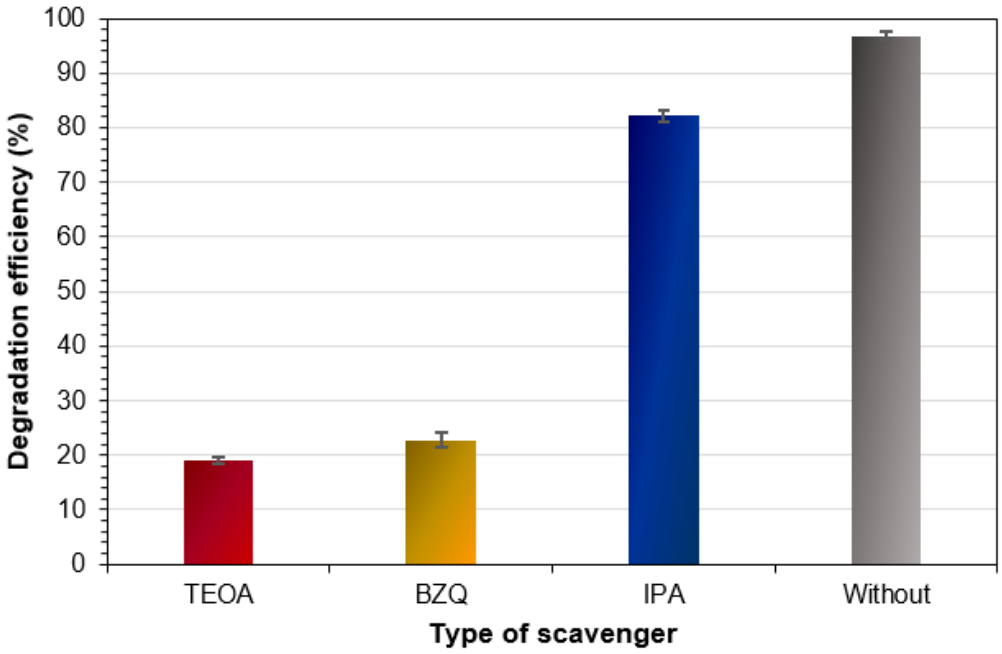

Fig. 9 (a) Summary of photocatalytic performance and (b) Graph of photodegradation efficiency displayed by 1-BCQD/CN in the presence of different scavengers

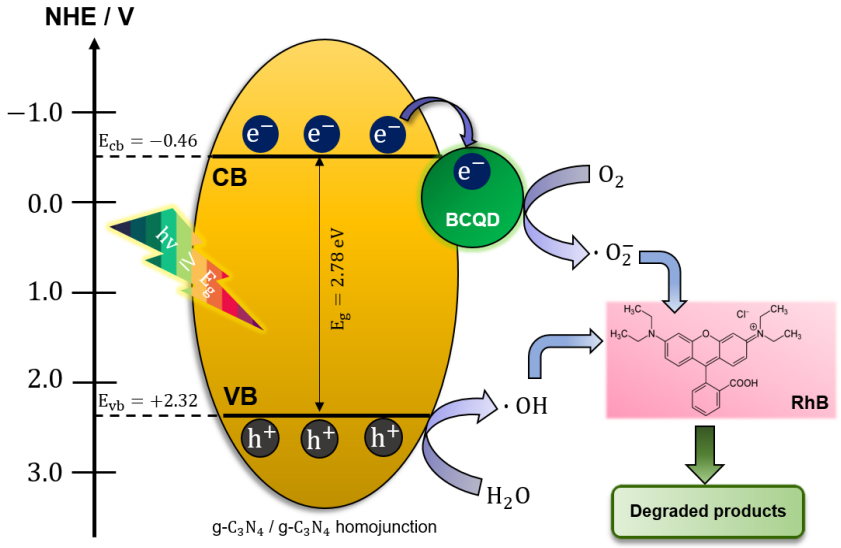

Fig. 10 Schematic illustration of the plausible photocatalytic mechanism and a series of photo-reaction chain for RhB dye degradation in the presence of CQD-based g-C_3N_4 as photocatalyst

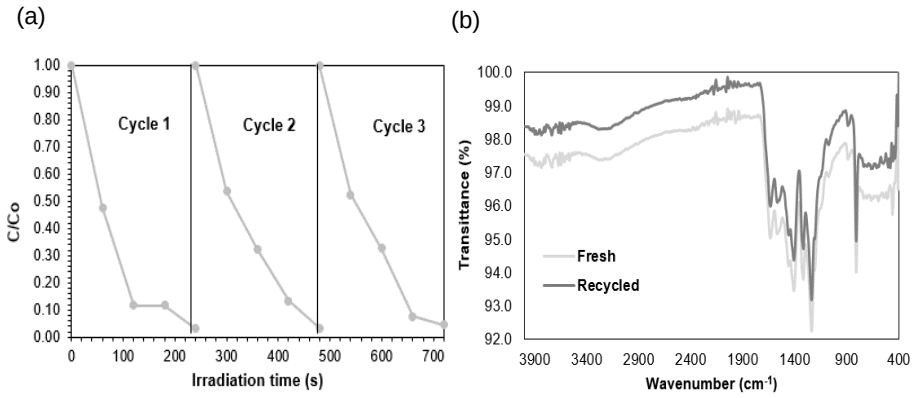

Fig. 11 (a) Recyclability test of 1-BCQD/CN for 3 consecutive cycles and (b) FTIR spectra of 1-BCQD/CN in fresh and recycled conditions

(a)

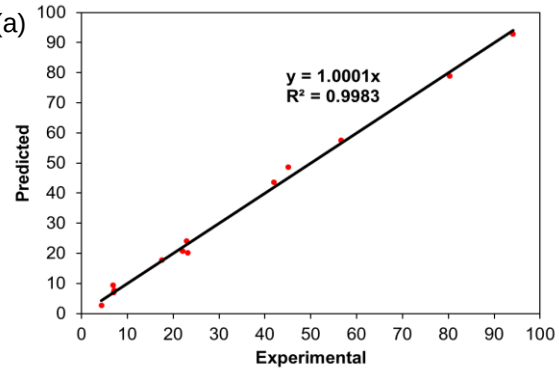

(b)

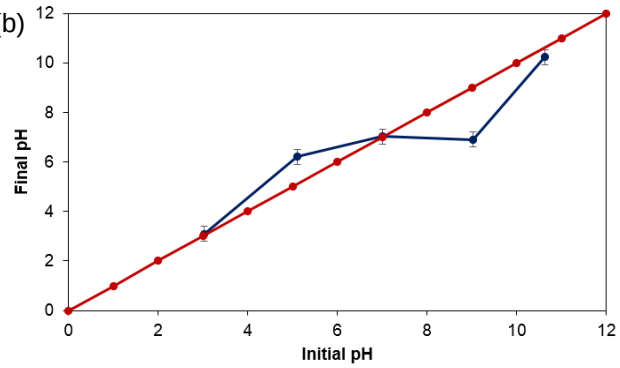

(c)

pH value	Initial dye concentration (mg/L)	Dosage of photocatalyst (g)	RhB photodegradation (%)	
			Experimental	Predicted
3.37	10	0.20	96.22	100

Fig. 12 (a) Graph of predicted against experimental data for each run, (b) Plot for determination of pH_{pzc} of 1-BCQD/CN and (c) Optimum conditions

Table

Table 1. Experimental level and range of the independent parameters

Variables	Level and range		
	-1	**0**	**+1**
pH value, x_1	3	7	11
Initial dye concentration, x_2 (mg/L)	10	20	30
Photocatalyst dosage, x_3 (g)	0.10	0.15	0.20

Table 2. Model summary for the regression model

Standard deviation	R^2	R^2 (Adjusted)	PRESS	R^2 (Predicted)
2.5528	99.56 %	99.12 %	309.996	97.01 %

PRESS: Prediction error sum of squares

Table 3. The set independent variables, experimental and predicted data for RhB degradation

Run order	Independent variables			Degradation of RhB (%)	
	x_1	x_2	x_3	Experimental	Predicted
1	11	20	0.10	6.866	9.498
2	11	20	0.20	17.544	17.782
3	7	30	0.10	4.373	2.644
4	3	30	0.15	41.903	43.593
5	7	20	0.15	22.054	20.776
6	3	20	0.10	56.646	57.574
7	7	10	0.10	22.892	24.120
8	11	10	0.15	23.132	20.219
9	7	30	0.20	7.073	7.702
10	11	30	0.15	7.036	7.061
11	3	10	0.15	94.102	92.847
12	7	10	0.20	45.043	48.638
13	3	20	0.20	80.330	78.866